Along-Track Swarm SAR: Echo Modeling and Sub-Aperture Collaboration Imaging Based on Sparse Constraints

Nan Jiang, Dong Feng, Jian Wang, Jiahua Zhu, and Xiaotao Huang, *Senior Member, IEEE*

***Abstract*—This article proposes an along-track swarm synthetic aperture radar (ATS-SAR) system to accomplish the high frame rate and enhance imaging resolution simultaneously. Unlike the current along-track multistatic SAR (Multi-SAR), each platform of the proposed ATS-SAR only collects part of the aperture data. Then, the bistatic pair acquisitions of ATS-SAR are transformed into virtual monostatic subapertures, and a large aperture is combined in a short time. Considering the practical motion state difference of each individual platform, various ATS-SAR echo models are thoroughly investigated and established. Furthermore, a subaperture collaboration imaging algorithm for ATS-SAR (SACIm-ATS) based on sparse constraints is also proposed. An effective phase compensation function is designed to improve echo sparsity by homogenizing the ATS-SAR echo. Then, the compressed sensing method can be utilized to accurately estimate more azimuth data, obtaining a higher azimuth resolution. Simulations and a real measured experiment are carried out to verify the effectiveness of the proposed ATS-SAR and the SACIm-ATS algorithm. Compared with the state-of-the-art imaging algorithms, the proposed SACIm-ATS algorithm can significantly enhance the ATS-SAR imaging performance.**

***Index Terms*—Along-track swarm SAR, compressed sensing, echo modeling, multistatic SAR (Multi-SAR), subaperture collaboration imaging.**

I. Introduction

SINCE it was first proposed in the 1960s, conventional monostatic SAR (Mono-SAR) has received much research in the sectors of civilian and national security [1], [2], [3]. With the advent of compressed sensing (CS) technology in recent decades, the prior information of imaging scene sparsity has been widely considered and fully utilized [4], [5]. The related SAR imaging algorithms based on sparse constraints have been rapidly investigated [6], [7], [8], so that the sparse targets such as ships and space targets can be well imaged with fewer data.

However, Mono-SAR has three inherent limitations. First, due to the minimum antenna area constraint, high resolution, and wide swath cannot be satisfied simultaneously with single-channel antenna [9]. Second, interferometric SAR (InSAR) imaging requires that Mono-SAR fly twice, reducing the performance of InSAR imaging [10]. Third, high resolution and high frame rate are inherently contradictory for Mono-SAR, resulting in a long data collection time. Therefore, multistatic SAR (Multi-SAR) was proposed in the early 1990s [11], [12]. The transmitters and receivers are separated in Multi-SAR, achieving better concealment and flexibility [13]. However, the primary purpose of almost all Multi-SAR is to address the first and second inherent limitations of Mono-SAR. All platforms must collect the complete synthetic aperture data to ensure high azimuth resolution, leading to a long data collection time and a low frame rate.

With the rapid development of unmanned aerial vehicles (UAV) swarm [14], [15], Fang initially proposed a preliminary concept of a high frame rate UAV swarm SAR in order to tackle the third inherent problem of Mono-SAR [16]. The one-transmitter-N-receiver high frame rate UAV swarm SAR is separated into N bistatic pairs and is equivalent to N virtual Mono-SAR on the angle bisector of the target's view. Small subapertures are captured concurrently via multiple platforms in a short period of time, merging a larger synthetic aperture to improve azimuth resolution. Due to its short data acquisition time, the SAR system is more concealed and has a preferable anti-interference ability. Therefore, this UAV swarm SAR can be regarded as an enhanced configuration of the existing SAR system. Almost all the application backgrounds of the existing SAR system apply to it, especially in the case of long data collection time. However, it exposes several problems.

1) It does not inspire the most efficient mode of UAV swarm SAR. After the bistatic-monostatic transformation, the length of the combined equivalent aperture will be less than that of the UAV swarm SAR's total running distance. Thus, it moves longer but obtains a low-quality azimuth resolution. It could be more efficient, especially for the sparse targets.
2) The practical motion state of each individual platform is ignored. It assumes that all drones are flying at the same speed, but this is only the case in a perfect formation. The velocity difference of platforms will result in

Manuscript received 9 January 2023; revised 25 February 2023, 23 March 2023, and 22 May 2023; accepted 11 June 2023. Date of publication 14 June 2023; date of current version 28 June 2023. This work was supported by the National Natural Science Foundation of China under Grant 62101562. *(Corresponding author: Dong Feng.)*

Nan Jiang, Dong Feng, Jian Wang, and Xiaotao Huang are with the College of Electronic Science and Technology, National University of Defense Technology, Changsha 410073, China (e-mail: jiangnan@nudt.edu.cn; fengdong09@nudt.edu.cn; hurri_can@163.com; xthuang@nudt.edu.cn).

Jiahua Zhu is with the College of Meteorology and Oceanography, National University of Defense Technology, Changsha 410073, China (e-mail: zhujiahua1019@hotmail.com).

Digital Object Identifier 10.1109/JSTARS.2023.3286068

different sampling intervals in different virtual subapertures, forming a nonuniform sampling aperture signal.

Meanwhile, it may cause certain gaps between virtual subapertures, resulting in missing Doppler data. A lack of Doppler data will result in azimuth aliasing and a substantial degradation in imaging performance.

In order to address the third inherent limitation of Mono-SAR and solve the problems of the high frame rate UAV swarm SAR, a novel along-track swarm SAR (ATS-SAR) concept is proposed in this article. First, the proposed ATS-SAR can maintain a high-quality azimuth resolution even with short runs. Meanwhile, the proposed ATS-SAR considers a more general case: each platform moves at a different speed. It is common in practice, for example, when the ATS-SAR comprises of several platform types and some of those platforms need to move at various speeds to minimize interference and detection. The main difference between ATS-SAR and current along-track Multi-SAR [17], [18], [19] is that: instead of acquiring the complete aperture data, every platform of ATS-SAR only collects part of the aperture data to combine a large synthetic aperture. More concretely, in the ideal formation case, N platforms of ATS-SAR move together with the same velocity, forming N-segment virtual subapertures. Thus, compared with the conventional Mono-SAR, the data collection time of ATS-SAR is significantly reduced. Furthermore, since fewer data are required for imaging in the sparse case, the data collection time can be further reduced [20]. It is worth mentioning that the proposed ATS-SAR is not restricted to the case of UAV swarms. Also covered are the airborne and spaceborne swarm SARs.

If the full aperture of ATS-SAR is utilized for imaging, the optimal azimuth resolution can be obtained. However, due to the motion state difference of ATS-SAR's platforms, the effective aperture data of the combined aperture will be much less than that of the full aperture. Therefore, motivated by the Mono-SAR data recovery imaging algorithm, we try to collaboratively estimate the complete aperture data from the subapertures in ATS-SAR. In 2018, Qian proposed an Azimuth Missing Data Imaging Algorithm (AMDIA) based on sparse constraints for Mono-SAR [21]. The AMDIA reconstructs a phase-compensated complete echo at the Doppler domain based on the generalized orthogonal matching pursuit (gOMP) algorithm [22]. Then, the reconstructed signal transfers to the 2-D time domain after a phase compensation step to obtain the estimated complete echo. Finally, the conventional SAR imaging algorithms can obtain an accurate image with the estimated complete echo. Thanks to the low computational burden and robustness of the echo signal-to-noise ratio (SNR), the AMDIA has been developed rapidly in recent years. Liu extended it into spaceborne azimuth interrupted FMCW SAR and obtained an obvious imaging performance improvement [23], [24]. Wu provided an improved AMDIA via sparsity adaptive segmented orthogonal matching pursuit (StOMP) algorithm [25]. Compared with [21], it no longer needs to clarify the imaging sparsity, improving the imaging performance without the prior sparsity information. Aiming at the dechirped Azimuth Missing Data SAR (AMD-SAR) imaging problem, we proposed an improved AMDIA based on 2-D frequency domain recovery [26]. It has two advantages. First, the computational complexity of proposed algorithm is reduced since just the range gate signal where the target is located needs to be recovered. Additionally, it is possible to improve imaging performance by reducing the signal reconstruction errors.

If all platforms of ATS-SAR move with identical velocities, the ATS-SAR echo can be regarded as a uniform sampling Mono-SAR AMD echo. However, the velocity difference complicates the echo model. The azimuth sampling interval of each platform becomes nonuniform. Since the state-of-art AMDIA (SOA-AMDIA) can only address the uniform sampling situation, it cannot be directly applied to ATS-SAR imaging in complex formation cases. Therefore, the ideal and complex formation ATS-SAR cases are carefully investigated. The more realistic ATS-SAR echo models are established. Moreover, motivated by the SOA-AMDIA, a virtual Sub-Apertures Collaboration Imaging algorithm for ATS-SAR (SACIm-ATS) algorithm based on the sparse constraints is proposed. First, the ATS-SAR echo is homogenized by analyzing the greatest common divisor of all platforms' velocities. The effective azimuth samples are projected onto the positions corresponding to the homogenized uniform sampling echo. Indeed, the homogenized uniform sampling echo is incomplete. Furthermore, a phase compensation function (PCF) is designed based on the newly constructed echo to ensure a sparsity representation at the Doppler domain. To eliminate the potential error effects of different CS methods, the gOMP algorithm [22] is also chosen to collaboratively estimate the complete aperture data in SACIm-ATS, as in the SOA-AMDIA [21], [23], [24], [26], [27], [28]. Finally, the ATS-SAR imaging scene can be well-focused with the estimated full aperture even in the complex formation cases.

The main innovations and contributions of the article are as follows:

1) We first propose ATS-SAR in this article to address the third inherent limitation of Mono-SAR and solve the problems of the SOA UAV swarm SAR. Moreover, the proposed ATS-SAR considers the practical motion state of each individual platform. Multiple complex ATS-SAR echo models are first established.
2) We first propose a subaperture collaboration imaging algorithm, SACIm-ATS, to address the ATS-SAR imaging problem. The greatest common divisor of each platform's velocity is applied to homogenize the nonuniform ATS-SAR echo, and an effective PCF is designed to improve estimation accuracy of the full aperture data. The SOA-AMDIA can be regarded as a particular case of the proposed SACIm-ATS when the velocities of all platforms are identical. Hence, the proposed SACIm-ATS extends the applicable scope of the SOA-AMDIA.
3) To validate the effectiveness of the proposed SACIm-ATS in the real scene, an artificial ATS-SAR experiment is generated from a real measured Mono-SAR data. Compared with the SOA imaging algorithms, the proposed SACIm-ATS algorithm can significantly enhance the ATS-SAR imaging performance.

The article is organized as follows: in Section II, the echo models of the ATS-SAR are described and analyzed in detail. In

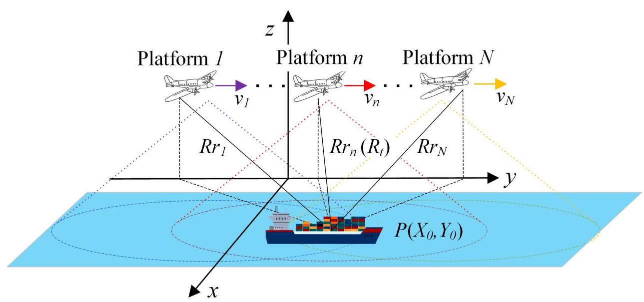

Fig. 1. Geometric configuration of ATS-SAR.

Section III, the proposed SACIm-ATS is introduced and derived. In Section IV, the simulations are designed, and the results are analyzed in detail. In Section V, an artificial ATS-SAR experiment based on the real Mono-SAR data is carried out and the results are illustrated and analyzed. Finally, Section VI gives the conclusion.

II. ATS-SAR Echo Modeling

Suppose an $N (N \geq 2)$ platforms ATS-SAR consists of one transmitter and N receivers. The geometric configuration is shown in Fig. 1. The slant range between the nth receiver and the sparse target $P(X_0, Y_0)$ is denoted by R_{r_n}. The moving velocity of the nth platform is represented by v_n. The received ATS-SAR echo geometric model is demonstrated in Fig. 2. y_n denotes the initial position of the nth platform, and L_{fa} denotes the length of full aperture.

In the ideal formation case, all platforms simultaneously move with the same velocity v. Considering the balance between data collection time and effective data amount, the moving distance of each platform equals $L_{fa}/2\ N$, and the interval between the adjacent platforms equals L_{fa}/N. The data collection time t_{SA} and the pulse repetition frequency (PRF) F_a are identical. Thus, the azimuth samples number $M_{SA} = t_{SA} F_a$ of each platform are equivalent. The transmitted chirp signal $\boldsymbol{s}_t(t)$ is written as

$$s_t(t) = \beta_t w_r(t) \exp\left(j 2\pi f_c t\right) \exp\left(j\pi K_r t^2\right) \tag{1}$$

where t represents the elapsed time of the chirp signal, often known as fast time. K_r, f_c, β_t, and w_r represent the chirp rate, carrier frequency, chirp signal's amplitude, and range windowing function, respectively. After decarrier processing, the nth echo $\boldsymbol{s}_{r_n}$ is expressed as

$$\begin{aligned} s_{r_n}(t,\eta) = \beta_{r_n} w_r &\left(t - \frac{R_t(\eta) + R_{r_n}(\eta)}{c}\right) w_a(\eta) \\ &\times \exp\left(-\frac{j2\pi f_c \left(R_t(\eta) + R_{r_n}(\eta)\right)}{c}\right) \\ &\times \exp\left(j\pi K_r \left(t - \frac{R_t(\eta) + R_{r_n}(\eta)}{c}\right)^2\right) + n_0 \end{aligned} \tag{2}$$

where η stands for the time along with the synthetic aperture, often known as slow time. The azimuth windowing function is shown by w_a, while c stands for light speed and n_0 represents random noise. In the following derivation, the back-scattered coefficient β_{r_n} can be neglected. The slant range between the transmitter and $P(X_0, Y_0)$ is denoted by $R_t(\eta)$. Thus, the total slant range is written as

$$\begin{aligned} R_t(\eta) + R_{r_n}(\eta) &= \sqrt{{R_0}^2 + \left(y_t + v_t\eta - Y_0\right)^2} \\ &\quad + \sqrt{{R_0}^2 + \left(y_n + v_n\eta - Y_0\right)^2} \end{aligned} \tag{3}$$

where R_0 denotes the shortest slant range of $P(X_0, Y_0)$. y_n and y_t denote the initial azimuth coordinate of the nth platform and the transmitter, respectively. v_t represents the moving velocity of the transmitter and v_n stands for the moving velocity of the nth platform.

Assuming the initial interval I_n between the nth received platform and the transmitted platform equals $y_n - y_t$, then the Taylor approximation expansion of (3) becomes

$$\begin{aligned} R_t(\eta) + R_{r_n}(\eta) &\approx 2R_0 + \frac{\left(\left(v_n - v_t\right)\eta + I_n\right)^2}{4R_0} \\ &\quad + \frac{\left(\left(y_t + I_n/2\right) + \eta\left(v_n + v_t\right)/2 - Y_0\right)^2}{R_0}. \end{aligned} \tag{4}$$

The ATS-SAR can be interpreted as the combination of multiple bistatic pairs. Using the displaced phase center antenna (DPCA) technology, the ATS-SAR creates N equivalent phase centers, which can also be considered N virtual Mono-SAR [29], [30]. The initial azimuth coordinate and velocity of the nth virtual Mono-SAR are equal to $y_{vir_n} = y_t + I_n/2$ and $v_{vir_n} = (v_n + v_t)/2$, respectively. Hence, the azimuth sampling interval of the nth virtual Mono-SAR $d_{vir_n} = v_{vir_n}/F_a$. The length of the nth virtual aperture $L_{vir_n} = v_{vir_n} t_{SA}$. The virtual slant range $R_{vir_n}(\eta)$ can be expressed as

$$\begin{aligned} R_{vir_n}(\eta) &= \sqrt{{R_0}^2 + \left(y_{vir_n} + v_{vir_n}\eta - Y_0\right)^2} \\ &\approx R_0 + \frac{\left(y_{vir_n} + v_{vir_n}\eta - Y_0\right)^2}{2R_0}. \end{aligned} \tag{5}$$

By comparing (4) and (5), a phase error $\Delta\varphi$ is generated by

$$\begin{aligned} \Delta\varphi &= \frac{2\pi}{\lambda}\left(\left(R_t(\eta) + R_{r_n}(\eta)\right) - 2R_{vir_n}(\eta)\right) \\ &= \frac{\pi\left(\left(v_n - v_t\right)\eta + I_n\right)^2}{2\lambda R_0} \end{aligned} \tag{6}$$

where λ denotes wavelength. In the far-field assumption situation, since $v_n - v_t$ and I_n are far less than R_0, the defocus effect of $\Delta\varphi$ can be ignored. Moreover, according to the Taylor approximation expansion principle, the higher the order of expansion, the smaller the error between them. Therefore, the second-order expansion is accurate enough in the far-field case. However, if the ATS-SAR works in the near-field case, the phase error $\Delta\varphi$ cannot be ignored. Hence, $\Delta\varphi$ should be compensated to complete the bistatic-monostatic transformation. The far-field and near-field standards of the ATS-SAR are derived in detail in the Appendix. Furthermore, the applicability of the expansion item is also discussed in the Appendix.

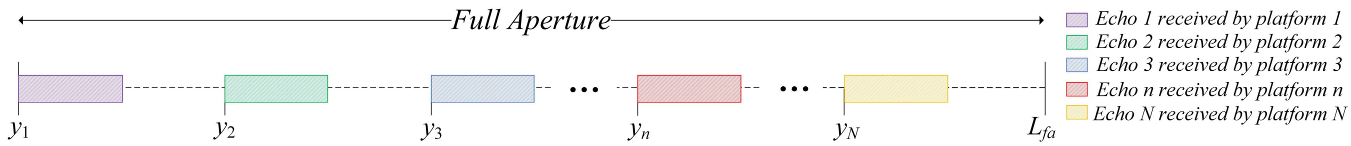

Fig. 2. Echo geometric model of the ATS-SAR. The rectangles with different colors represent different echoes of different platforms.

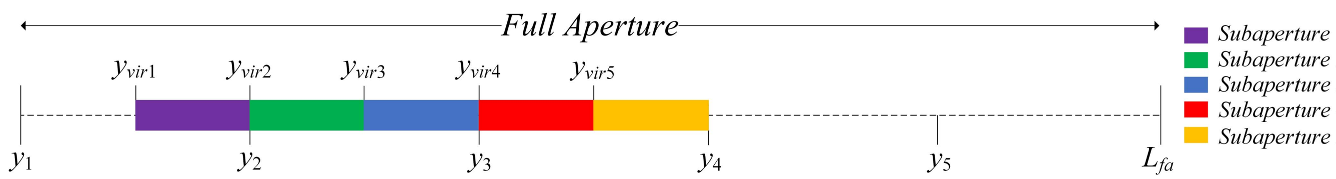

Fig. 3. Virtual echo geometry model of the ideal formation case. The rectangles with different colors represent different virtual subapertures.

After the bistatic–monostatic transformation, the nth virtual subaperture echo $\boldsymbol{s}_{vir_n}$ can be expressed as

$$\begin{aligned} s_{vir_n}(t,\eta) &= w_r\left(t-\frac{2R_{vir_n}(\eta)}{c}\right)w_a(\eta) \\ &\times \exp\left(-\frac{j4\pi f_c R_{vir_n}(\eta)}{c}\right) \\ &\times \exp\left(j\pi K_r\left(t-\frac{2R_{vir_n}(\eta)}{c}\right)^2\right)+n_0. \end{aligned} \tag{7}$$

Next, $\boldsymbol{s}_{vir_n}$ should be directly combined in sequence and the combined echo $\boldsymbol{s}_{cmb}$ is expressed as

$$\boldsymbol{s}_{cmb} = \lfloor \boldsymbol{s}_{vir_1}, \ldots, \boldsymbol{s}_{vir_n}, \ldots \boldsymbol{s}_{vir_N} \rfloor \tag{8}$$

where $\lfloor \cdot \rfloor$ denotes the combination operation. The size of $\boldsymbol{s}_{cmb}$ is $M_R \times NM_{SA}$, where M_R represents the number of the range samples.

However, since the motion state of each platform may be different, not all azimuth data in $\boldsymbol{s}_{cmb}$ are effective for ATS-SAR imaging. The effective signal $\boldsymbol{s}_{ef}$ consisting of the effective azimuth data may be distinct from $\boldsymbol{s}_{cmb}$. Thus, the ATS-SAR echo models should be examined further in the parts that follow. Moreover, for reasons of clearness, we skipped the derivation of multiple input multiple output (MIMO) ATS-SAR since it can be easily extended from the single input multiple output (SIMO) case.

A. *Ideal Formation Case:* $y_{vir_n} - y_{vir_{n-1}} = L_{vir_{n-1}}$

The motion state of ATS-SAR is considered ideal when $y_{vir_n} - y_{vir_{n-1}} = L_{vir_{n-1}}, n = 2, 3, \ldots, N$ happens. In the ideal formation case, $\boldsymbol{s}_{vir_n}$ are closely connected in turn. The virtual echo geometric model is shown in Fig. 3.

In this case, $\boldsymbol{s}_{ef}$ is identical to $\boldsymbol{s}_{cmb}$. However, in ATS-SAR, the received effective signal $\boldsymbol{s}_{ef}$ is not space-time equivalent. Therefore, the first step is to reconstruct a space-time equivalent signal $\boldsymbol{s}_{pf}$ using $\boldsymbol{s}_{ef}$. Since the ATS-SAR only collects part of azimuth data, some azimuth positions in $\boldsymbol{s}_{pf}$ do not have valid data. Thus, the ATS-SAR echo model $\boldsymbol{s}_{pf}$ is established and a position-finding step is defined. The azimuth samples of $\boldsymbol{s}_{ef}$ are determined in $\boldsymbol{s}_{pf}$ by multiplying a position-finding matrix $\boldsymbol{\Lambda}_{pf}$, which can be expressed as

$$\boldsymbol{s}_{pf} = \boldsymbol{s}_{ef}\boldsymbol{\Lambda}_{pf}. \tag{9}$$

Obviously, $\boldsymbol{s}_{pf}$ is regarded as the ATS-SAR echo filled with only $\boldsymbol{s}_{ef}$, and the data before and after $\boldsymbol{s}_{ef}$ are zero-padding, as Fig. 3 shown. The sizes of $\boldsymbol{s}_{pf}$ and $\boldsymbol{s}_{ef}$ are equal to $M_R \times M_{PF}$ and $M_R \times NM_{SA}$, respectively, where M_{PF} represents the azimuth samples number of $\boldsymbol{s}_{pf}$. The position-finding matrix $\boldsymbol{\Lambda}_{pf}$ can be expressed as

$$\boldsymbol{\Lambda}_{pf} = \begin{bmatrix} \mathbf{0} & \boldsymbol{I}_{NM_{SA}} & \mathbf{0} \end{bmatrix} \tag{10}$$

where $\boldsymbol{I}_{NM_{SA}}$ is an identity matrix and its size equals NM_{SA}. Obviously, $\boldsymbol{\Lambda}_{pf}$ is designed to obtain a longer signal $\boldsymbol{s}_{pf}$ using a shorter signal $\boldsymbol{s}_{ef}$. Hence, the column number of $\boldsymbol{\Lambda}_{pf}$ is larger than its row number. The 2-D size of $\boldsymbol{\Lambda}_{pf}$ equals $NM_{SA} \times M_{PF}$. Assuming the zero matrices before and after $\boldsymbol{s}_{ef}$ are generated by virtual subaperture 1 and virtual subaperture N, respectively. Thus, the size of the former and the latter zero matrix in $\boldsymbol{\Lambda}_{pf}$ equal $NM_{SA} \times (y_{vir_1} - y_1)/d_{vir_1}$ and $NM_{SA} \times (L_{fa} - (y_{vir_N} + L_{vir_N}))/d_{vir_N}$.

Overall, the ATS-SAR echo model $\boldsymbol{s}_{pf}$ is obtained in the ideal formation case. It is an azimuth uniform sampling signal. The fast time of $\boldsymbol{s}_{pf}$ is still t. The slow time axis η_{pf} becomes an axis of length M_{PF}, where $M_{PF} = 2NM_{SA}$.

B. *Complex Formation Cases:* $y_{vir_n} - y_{vir_{n-1}} \neq L_{vir_{n-1}}$

In fact, it is difficult to ensure that the speed of each radar platform is same, namely $y_{vir_n} - y_{vir_{n-1}} \neq L_{vir_{n-1}}$. In the meantime, assuming that L_{vir_n} difference is constrained to fall inside a certain range $L_{vir_n} \in (0, L_{fa}/N)$. Next, the ATS-SAR echo models are then investigated in further detail under multiple challenging situations.

1) Complex Formation Case 1: $y_{vir_n} - y_{vir_{n-1}} > L_{vir_{n-1}}$: In this case, the virtual subaperture echoes are no longer tightly connected anymore. The virtual echo geometric model is demonstrated in Fig. 4. Observing Fig. 4 reveals that $\boldsymbol{s}_{ef} = \boldsymbol{s}_{cmb}$. The position-finding steps for ideal formation and complex formation case 1 are comparable. The ATS-SAR echo $\boldsymbol{s}_{pf}$ for

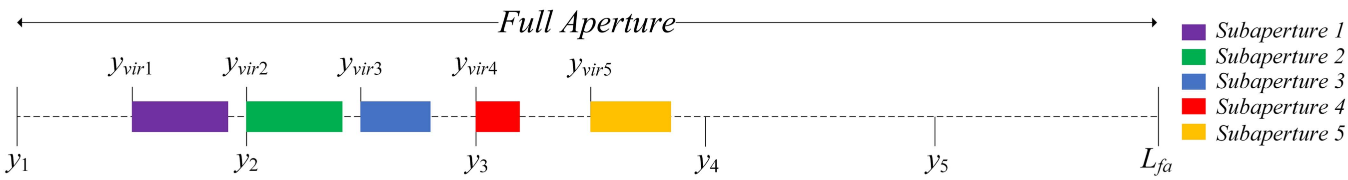

Fig. 4. Virtual echo geometric model in the case of complex formation case 1. The rectangles with different colors represent different virtual subapertures.

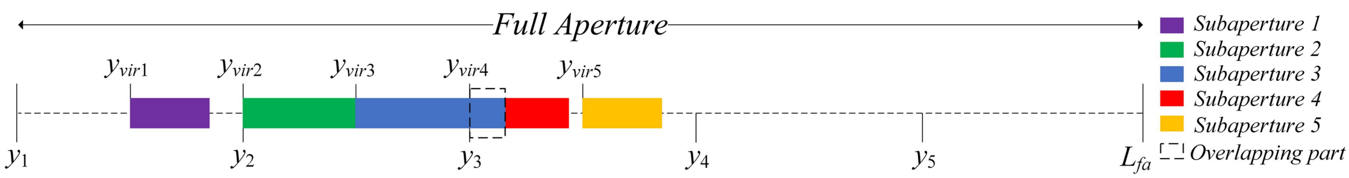

Fig. 5. Virtual echo geometric model in the case of complex formation case 2. The rectangles with different colors represent different virtual subapertures.

complex formation case 1 can be obtained by

$$\boldsymbol{s}_{pf} = \boldsymbol{s}_{ef}\widetilde{\boldsymbol{\Lambda}}_{pf1}. \tag{11}$$

Assume the gap between y_{vir_n} and $y_{vir_{n-1}}$ is created by the $(n-1)$th virtual subaperture, while the beginning and ending gaps are caused by the first and Nth virtual subapertures, respectively. Thus, the position-finding matrix $\widetilde{\boldsymbol{\Lambda}}_{pf1}$ is expressed as

$$\widetilde{\boldsymbol{\Lambda}}_{pf1} = \begin{bmatrix} \mathbf{0} & \widetilde{\boldsymbol{I}}_{NM_{SA}} & \mathbf{0} \end{bmatrix} \tag{12}$$

The size of the zero matrices in (12) is identical to that in the ideal formation case. Compared with (10), since there are gaps between the virtual subapertures, as Fig. 4 shown, the identity matrix $\boldsymbol{I}_{NM_{sa}}$ of (10) should be unfolded and filled with some zero matrices. Thus, the deformed matrix $\widetilde{\boldsymbol{I}}_{NM_{SA}}$ is not a square matrix anymore and is demonstrated as

$$\widetilde{\boldsymbol{I}}_{NM_{SA}} = \begin{bmatrix} \boldsymbol{\psi}_1 & & & & \mathbf{0} \\ & \ddots & & & \\ & & \boldsymbol{\psi}_2 & & \\ & & & \ddots & \\ \mathbf{0} & & & & \boldsymbol{\psi}_N \end{bmatrix} \tag{13}$$

where $\boldsymbol{\psi}_n = \boldsymbol{I}_{M_{SA}}$. The size of each zero matrix is related to the gap size, which is equal to $NM_{SA} \times (y_{vir_n} - (y_{vir_{n-1}} + L_{vir_{n-1}}))/d_{vir_{n-1}}$.

Therefore, the ATS-SAR echo model $\boldsymbol{s}_{pf}$ is an azimuth nonuniform sampling signal when the complex formation case 1 happens. The number of the azimuth samples M_{PF} can be calculated by

$$M_{PF} = \frac{y_{vir_1}}{d_{vir_1}} + \sum_{n=2}^{N+1} M_{vir_{n-1}} \tag{14}$$

where $M_{vir_{n-1}}$ is expressed as

$$M_{vir_{n-1}} \triangleq \frac{y_{vir_n} - y_{vir_{n-1}}}{d_{vir_{n-1}}} \tag{15}$$

and $y_{vir_{N+1}} = L_{fa}$.

2) Complex Formation Case 2: $L_{vir_{n-1}} - L_{vir_n} < y_{vir_n} - y_{vir_{n-1}} < L_{vir_{n-1}}$: When situation $L_{vir_{n-1}} - L_{vir_n} < y_{vir_n} - y_{vir_{n-1}} < L_{vir_{n-1}}$ occurs, the initial azimuth position of the nth virtual Mono-SAR is smaller than the stop azimuth position of the $(n-1)$th virtual Mono-SAR. Hence, the overlapping azimuth data are inevitable, as shown in Fig. 5. Obviously, part data of virtual subaperture 3 overlaps the data of virtual subaperture 4, which indicates that the $L_{vir_3} - L_{vir_4} < y_{vir_4} - y_{vir_3} < L_{vir_3}$.

We assume that the overlapping data are redundantly collected by the previous virtual subaperture. Thus, to remove the redundant data, an operator $\Omega\{n\}$ is defined to determine and select the value of n which satisfies the complex formation case 2. This step can be expressed as

$$n = \Omega\left\{L_{vir_{n-1}} - L_{vir_n} < y_{vir_n} - y_{vir_{n-1}} < L_{vir_{n-1}}\right\}. \tag{16}$$

n satisfying (16) is selected and put into a set $\boldsymbol{Z}_{OL}$. The elements number of $\boldsymbol{Z}_{OL}$ is equal to N_{OL}. Obviously, in the complex formation case 2, the effective signal $\boldsymbol{s}_{ef}$ in ATS-SAR is no longer identical to $\boldsymbol{s}_{cmb}$. The effective data selection step is then revised as

$$\boldsymbol{s}_{ef} = \boldsymbol{s}_{cmb}\widehat{\boldsymbol{I}}_{ef2} \tag{17}$$

where the deformed identity matrix $\widehat{\boldsymbol{I}}_{ef2}$ can be defined as

$$\widehat{\boldsymbol{I}}_{ef2} \triangleq \boldsymbol{I}\left(:, b_{ef2}(n)\right)|_{n \in \boldsymbol{Z}_{OL}} = \varnothing. \tag{18}$$

$\varnothing$ denotes the empty set and

$$b_{ef2}(n) \triangleq \left((n-2)\, M_{SA} + M_{vir_{n-1}} + 1\right) : (n-1)\, M_{SA}. \tag{19}$$

When complex formation case 2 occurs, the size of $\boldsymbol{s}_{ef}$ becomes $M_R \times M_{EF2}$. M_{EF2} denotes azimuth samples number of $\boldsymbol{s}_{ef}$, which can be obtained by

$$M_{EF2} = (N - N_{OL})\, M_{SA} + \sum_{n \in \boldsymbol{Z}_{OL}} M_{vir_{n-1}}. \tag{20}$$

The related position-finding step is expressed as

$$\boldsymbol{s}_{pf} = \boldsymbol{s}_{ef}\widetilde{\boldsymbol{\Lambda}}_{pf2} \tag{21}$$

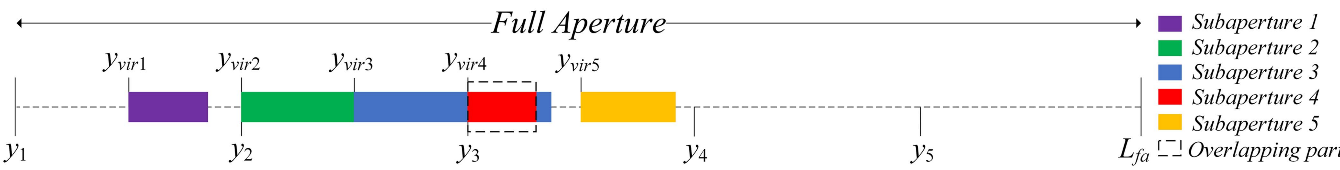

Fig. 6. Virtual echo geometric model in the case of complex formation case 3. The rectangles with different colors represent different virtual subapertures.

where $\widetilde{\boldsymbol{\Lambda}}_{pf2}$ is different from $\widetilde{\boldsymbol{\Lambda}}_{pf1}$ due to the change in quantity of the effective azimuth samples, that is

$$\widetilde{\boldsymbol{\Lambda}}_{pf2} = \begin{bmatrix} \mathbf{0} & \widetilde{\boldsymbol{I}}_{(N-N_{OL})M_{SA}} & \mathbf{0} \end{bmatrix} \tag{22}$$

The row number of $\widetilde{\boldsymbol{\Lambda}}_{pf2}$ equals M_{EF2}. Thus, the row numbers of the beginning and the ending zero matrices are equal to M_{EF2}. The column numbers of them are equal to $(y_{vir_1} - y_1)/d_{vir_1}$ and $(L_{fa} - (y_{vir_N} + L_{vir_N}))/d_{vir_N}$, respectively. Moreover, the deformed matrix $\widetilde{\boldsymbol{I}}_{(N-N_{OL})M_{SA}}$ is illustrated as

$$\widetilde{\boldsymbol{I}}_{(N-N_{OL})M_{SA}} = \begin{bmatrix} \widetilde{\boldsymbol{\psi}}_1 & & & & \mathbf{0} \\ & \ddots & & & \\ & & \widetilde{\boldsymbol{\psi}}_2 & & \\ & & & \ddots & \\ \mathbf{0} & & & & \widetilde{\boldsymbol{\psi}}_N \end{bmatrix} \tag{23}$$

where $\widetilde{\boldsymbol{\psi}}_{n-1}$ should be expressed as

$$\begin{cases} \widetilde{\boldsymbol{\psi}}_{n-1} = \boldsymbol{I}_{M_{EF2}}, & n \in \boldsymbol{Z}_{OL} \\ \widetilde{\boldsymbol{\psi}}_{n-1} = \boldsymbol{I}_{M_{SA}}, & \text{else.} \end{cases} \tag{24}$$

Obviously, $\widetilde{\boldsymbol{I}}_{(N-N_{OL})M_{SA}}$ is not a square matrix. Additionally, the sizes of zero matrices in (23) depend on the different situations. No zero matrix is filled in between $\widetilde{\boldsymbol{\psi}}_{n-1}$ and $\widetilde{\boldsymbol{\psi}}_n$ when $n \in \boldsymbol{Z}_{OL}$, and the size of the zero matrix between $\widetilde{\boldsymbol{\psi}}_{n-1}$ and $\widetilde{\boldsymbol{\psi}}_n$ equals $M_{EF2} \times (M_{vir_{n-1}} - M_{SA})$ under the else conditions.

Therefore, in this situation, ATS-SAR echo $\boldsymbol{s}_{pf}$ is also an azimuth nonuniform sampling signal. The calculation formula of M_{PF} is the same as (14).

3) Complex Formation Case 3: $0 < y_{vir_n} - y_{vir_{n-1}} \leq L_{vir_{n-1}} - L_{vir_n}$*:* When $0 < y_{vir_n} - y_{vir_{n-1}} \leq L_{vir_{n-1}} - L_{vir_n}$ occurs, ATS-SAR echo $\boldsymbol{s}_{pf}$ becomes more complicated. The physical meaning of complex formation case 3 is that the stop azimuth coordinate of the nth virtual Mono-SAR is even smaller than that of the $(n-1)$th virtual Mono-SAR. It also indicates that the nth virtual subaperture will be entirely enclosed within the $(n-1)$th virtual subaperture. This phenomenon can be observed more clearly in Fig. 6. The virtual subaperture 4 in red is contained by subaperture 3 in blue, which implies that the $0 < y_{vir_4} - y_{vir_3} \leq L_{vir_3} - L_{vir_4}$. Thus, $\Omega\{n\}$ is also utilized to erase the redundant data, that is

$$n = \Omega\left\{0 < y_{vir_n} - y_{vir_{n-1}} \leq L_{vir_{n-1}} - L_{vir_n}\right\}. \tag{25}$$

Then, the selected n is put into a set $\boldsymbol{Z}_{UL}$ and the elements number of $\boldsymbol{Z}_{UL}$ equals N_{UL}. The effective data selection step is demonstrated as

$$\boldsymbol{s}_{ef} = \boldsymbol{s}_{cmb}\widehat{\boldsymbol{I}}_{ef3}. \tag{26}$$

Compared with (18), the form of $\widehat{\boldsymbol{I}}_{ef3}$ is revised as

$$\widehat{\boldsymbol{I}}_{ef3} \triangleq \boldsymbol{I}\left(:, [(n-1)\, M_{SA} + 1 : nM_{SA}]\right)\big|_{n \in \boldsymbol{Z}_{UL}} = \varnothing. \tag{27}$$

Since the nth virtual subdata aperture's data are erased, the number of the virtual Mono-SAR equals $N - N_{UL}$. Accordingly, the size of $\boldsymbol{s}_{ef}$ changes to $M_R \times (N - N_{UL})M_{SA}$.

Then, the ATS-SAR echo $\boldsymbol{s}_{pf}$ can be expressed as

$$\boldsymbol{s}_{pf} = \boldsymbol{s}_{ef}\widetilde{\boldsymbol{\Lambda}}_{pf3} \tag{28}$$

where $\widetilde{\boldsymbol{\Lambda}}_{pf3}$ is revised as

$$\widetilde{\boldsymbol{\Lambda}}_{pf3} = \begin{bmatrix} \mathbf{0} & \widetilde{\boldsymbol{I}}_{(N-N_{UL})M_{SA}} & \mathbf{0} \end{bmatrix}. \tag{29}$$

The row number of $\widetilde{\boldsymbol{\Lambda}}_{pf3}$ equals $(N - N_{UL})M_{SA}$. Then, the sizes of the former and latter zero matrices in (29) equal $(N - N_{UL})M_{SA} \times (y_{vir_1} - y_1)/d_{vir_1}$ and $(N - N_{UL})M_{SA} \times (L_{fa} - (y_{vir_N} + L_{vir_N}))/d_{vir_N}$, respectively. The deformed matrix $\widetilde{\boldsymbol{I}}_{(N-N_{UL})M_{SA}}$ is illustrated as

$$\widetilde{\boldsymbol{I}}_{(N-N_{UL})M_{SA}} = \begin{bmatrix} \boldsymbol{\psi}_1 & & & & \mathbf{0} \\ & \ddots & & & \\ & & \boldsymbol{\psi}_2 & & \\ & & & \ddots & \\ \mathbf{0} & & & & \boldsymbol{\psi}_{N-N_{UL}} \end{bmatrix} \tag{30}$$

where $\boldsymbol{\psi}_n = I_{M_{SA}}$. The size of the zero matrix between the adjacent $\boldsymbol{\psi}_n$ equals $(N - N_{UL})M_{SA} \times (y_{vir_n} - (y_{vir_{n-1}} + L_{vir_{n-1}}))/d_{vir_{n-1}}$.

In complex formation case 3, ATS-SAR echo model $\boldsymbol{s}_{pf}$ is still an azimuth nonuniform sampling signal. The number of the azimuth samples M_{PF} can be calculated by

$$M_{PF} = \frac{y_{vir_1}}{d_{vir_1}} + \sum_{n=2}^{N+1} \frac{y_{vir_n} - y_{vir_{n-1}}}{d_{vir_{n-1}}} + \sum_{n \in \boldsymbol{Z}_{UL}} \left(\frac{y_{vir_{n+1}} - y_{vir_n}}{d_{vir_{n-1}}} - \frac{y_{vir_{n+1}} - y_{vir_n}}{d_{vir_n}} \right). \tag{31}$$

Finally, it is worth mentioning that the complex formation case 1, 2, and 3 may occur in the ATS-SAR at the same time.

C. Other Formation Cases

Despite the fact that the following conditions will not arise in the ATS-SAR described in this work, they are discussed in this part nonetheless. First, $y_{vir_n} - y_{vir_{n-1}}$ is always larger than 0 since y_n is always larger than y_{n-1}. Thus, $y_{vir_n} - y_{vir_{n-1}} \le 0$ will not be analyzed in the proposed ATS-SAR. Furthermore, due to $L_{vir_n} \in (0, L_{fa}/N)$, the maximum L_{vir_n} is less than $y_{vir_{n+2}} - y_{vir_n}$. There is no overlapping data between the nth virtual subaperture and the $(n+2)$th virtual subaperture. Therefore, it is no longer analyzed

III. Proposed ATS-SAR Collaboration Imaging Algorithm

Obviously, compared with the full aperture, the Doppler bandwidth of ATS-SAR echo is limited whether in the ideal or complex formation cases. To simultaneously obtain a high azimuth resolution and a high frame rate, the SACIm-ATS is proposed in this article. At first, the 2-D time domain ATS-SAR echo $\boldsymbol{s}_{pf}$ can be expressed as

$$\begin{aligned} s_{pf}(t,\eta_{pf}) &= w_r\left(t - \frac{2R_{pf}(\eta_{pf})}{c}\right) w_a(\eta_{pf}) \\ &\times \exp\left(-\frac{j4\pi f_c R_{pf}(\eta_{pf})}{c}\right) \\ &\times \exp\left(j\pi K_r\left(t - \frac{2R_{pf}(\eta_{pf})}{c}\right)^2\right) + n_0. \end{aligned} \tag{32}$$

The slant range $\boldsymbol{R}_{pf}$ can be demonstrated as

$$R_{pf}(\eta_{pf}) = \sqrt{{R_0}^2 + (y_1 + \widetilde{v}_{pf}\eta_{pf} - Y_0)^2} \tag{33}$$

where $\widetilde{v}_{pf}$ represents the velocity of virtual Mono-SAR, and $\widetilde{v}_{pf} = v_t$ in the ideal formation case. In the complex formation cases, $\widetilde{v}_{pf}$ is related to slow time η_{pf}, that is

$$\begin{cases} \widetilde{v}_{pf} = v_{vir_1},\ \eta_{pf} \in \left(0, \frac{y_{vir_2}}{v_{vir_1}}\right], & n=1 \\ \widetilde{v}_{pf} = v_{vir_n},\ \eta_{pf} \in \left(\frac{y_{vir_n}}{v_{vir_{n-1}}}, \frac{y_{vir_{n+1}}}{v_{vir_n}}\right], & n = 2,\ldots,N. \end{cases} \tag{34}$$

The interval $\widetilde{d}_{pf}$ between the adjacent azimuth samples can be illustrated by $\widetilde{d}_{pf} = \widetilde{v}_{pf}/F_a$. With no doubt, the nonuniform $\widetilde{d}_{pf}$ is not conducive to the estimation of full aperture data.

Concerning this, the greatest common divisor velocity is calculated and utilized to design a denser azimuth uniform sampling echo $\boldsymbol{s}_{um}$. A new interval parameter $\overline{d}_{vir}$ is obtained by $\overline{d}_{vir} = \overline{v}_{vir}/F_a$. Assume that M_A represents the number of azimuth samples in $\boldsymbol{s}_{um}$. Hence, $M_A = L_{fa}/\overline{d}_{vir}$ and the size of $\boldsymbol{s}_{um}$ equals $M_R \times M_A$.

Next, all azimuth data of $\boldsymbol{s}_{pf}$ should be located to the correct azimuth positions in $\boldsymbol{s}_{um}$. This step can be expressed as (35), which is shown at the bottom of this page.

Since $\boldsymbol{s}_{um}$ is substantially more dense than $\boldsymbol{s}_{pf}$, there are gaps $\Delta g_n = d_{vir_n}/\overline{d}_{vir}$ between samples when the data on $\boldsymbol{s}_{pf}$ are mapped to $\boldsymbol{s}_{um}$.

Currently, an uniform sampling signal $\boldsymbol{s}_{um}$ is successfully obtained from $\boldsymbol{s}_{pf}$ with the identical phase information. Assuming M_Z and M_{NZ} denote the number of zero and nonzero azimuth samples in $\boldsymbol{s}_{um}$, respectively. $\boldsymbol{P}_{NZ}$ represents the position set of the nonzero azimuth samples in $\boldsymbol{s}_{um}$. To extend Doppler bandwidth and obtain a higher resolution imaging result for ATS-SAR, the real values of zero samples in $\boldsymbol{s}_{um}$ are estimated from the nonzero samples, so as to obtain the complete echo $\boldsymbol{s}_u$.

Actually, $\boldsymbol{s}_u$ can be regarded as a complete echo, which is collected by a virtual Mono-SAR with velocity $\overline{v}_{vir}$, that is

$$\begin{aligned} s_u(t,\eta_u) = w_r&\left(t - \frac{2R_u(\eta_u)}{c}\right) w_a(\eta_u) \\ &\times \exp\left(-\frac{j4\pi f_c R_u(\eta_u)}{c}\right) \\ &\times \exp\left(j\pi K_r\left(t - \frac{2R_u(\eta_u)}{c}\right)^2\right) + n_0 \end{aligned} \tag{36}$$

where the slant range $\boldsymbol{R}_u$ can be expressed as

$$R_u(\eta_u) = \sqrt{{R_0}^2 + (y_1 + \overline{v}_{vir}\eta_u - Y_0)^2} \tag{37}$$

η_u is identical to η_{um}, thus η_{um} is replaced by η_u in the following derivation for the sake of clarity. The relationship between $\boldsymbol{s}_u$ and $\boldsymbol{s}_{um}$ can be illustrated as

$$\boldsymbol{s}_{um} = \boldsymbol{s}_u \boldsymbol{\Lambda}_m \tag{38}$$

where $\boldsymbol{\Lambda}_m$ is a diagonal matrix which can be written as

$$\boldsymbol{\Lambda}_m = \mathrm{diag}\left[\lambda_1, \ldots, \lambda_{m_a}, \ldots, \lambda_{M_A}\right],\ m_a = 1, 2, \ldots, M_A \tag{39}$$

and

$$\begin{cases} \lambda_{m_a} = 1, & m_a \in \boldsymbol{P}_{NZ} \\ \lambda_{m_a} = 0, & \text{else}. \end{cases} \tag{40}$$

Obviously, $\boldsymbol{s}_u$ does not meet the requirement for sparsity in the 2-D time domain. However, motivated by the motion compensation step of the Polar Format algorithm, the echo signal can be much sparser in the Doppler domain by multiplying the echo signal and a PCF in the range frequency domain. The PCF $\boldsymbol{\theta}_{pc}$

$$\begin{cases} s_{um}\left(:, 1 : \Delta g_1 : \frac{y_{vir_2}}{\overline{d}_{vir}} - 1\right) = s_{pf}\left(:, 1 : \frac{y_{vir_2}}{d_{vir_1}} - 1\right), & n = 1 \\ s_{um}\left(:, \frac{y_{vir_n}}{\overline{d}_{vir}} : \Delta g_n : \frac{y_{vir_{n+1}}}{\overline{d}_{vir}} - 1\right) = s_{pf}\left(:, \sum_{n=2}^{n} \frac{y_{vir_n}}{d_{vir_{n-1}}} : \sum_{n=2}^{n+1} \frac{y_{vir_n}}{d_{vir_{n-1}}} - 1\right), & n = 2, \ldots, N-1 \\ s_{um}\left(:, \frac{y_{vir_N}}{\overline{d}_{vir}} : \Delta g_N : end\right) = s_{pf}\left(:, \frac{y_{vir_N}}{d_{vir_{N-1}}} : end\right), & n = N. \\ s_{um}(:, else) = 0 \end{cases} \tag{35}$$

is designed as

$$\theta_{pc}\left(f_r, \eta_u\right) = \exp\left(\frac{j\pi f_r^2}{K_r}\right) \exp\left\{\frac{j4\pi\left(f_c + f_r\right) R_{pc}\left(\eta_u\right)}{c}\right\} \tag{41}$$

where f_r denotes the range frequency. $\boldsymbol{R}_{pc}$ is the instantaneous distance between a phase compensation point and the moving virtual Mono-SAR, which is expressed as

$$R_{pc}\left(\eta_u\right) = \sqrt{R_{0,pc}^2 + \left(y_1 + \overline{v}_{vir}\eta_u - Y_{pc}\right)^2} \tag{42}$$

where the phase compensation point's shortest instantaneous distance and azimuth position are denoted by $R_{0,pc}$ and Y_{pc}, respectively.

In order to successfully exploit the CS-based method, a small size signal $s_{yum}(t, \eta_u)$ should be obtained by deleting all zero column vectors from $\boldsymbol{s}_{um}$, which can be expressed as

$$\boldsymbol{s}_{yum} = \boldsymbol{s}_{um}\widehat{\boldsymbol{I}}_y \tag{43}$$

where $\widehat{\boldsymbol{I}}_y$ is a deforming identity matrix and defined as

$$\widehat{\boldsymbol{I}}_y \triangleq \boldsymbol{I}\left(:, m_a\right)|_{m_a \notin \boldsymbol{P}_{NZ}} = \varnothing. \tag{44}$$

The size of $\boldsymbol{s}_{yum}$ equals $M_R \times M_{NZ}$. Accordingly, the small sized PCF $\boldsymbol{\theta}_{ypc}$ can also be obtained by removing zero column vectors of $\boldsymbol{\theta}_{mpc}$, which can be expressed as

$$\boldsymbol{\theta}_{ypc} = \boldsymbol{\theta}_{pc}\boldsymbol{\Lambda}_m\widehat{\boldsymbol{I}}_y. \tag{45}$$

Then, the phase compensated small size signal $\boldsymbol{S}_{ypc}$ can be obtained by

$$\boldsymbol{S}_{ypc} = \boldsymbol{S}_{yum}\boldsymbol{\theta}_{ypc} \tag{46}$$

while the phase compensated complete echo $\boldsymbol{S}_{pc}$ can be obtained by

$$\boldsymbol{S}_{pc} = \boldsymbol{S}_u\boldsymbol{\theta}_{pc}. \tag{47}$$

SACIm-ATS's primary purpose is to recover a sparse azimuth-frequency signal $\boldsymbol{S}_{pc}(t, f_a)$ from $\boldsymbol{s}_{ypc}(t, \eta_u)$ using the gOMP method, where f_a represents the azimuth frequency. The $\boldsymbol{s}_{ypc}$ matrix must be divided into M_R signal vectors corresponding to each range cell because the gOMP is a 1-D reconstruction approach. The qth signal vector can be expressed as $\boldsymbol{s}_{ypc}(t_q, \eta_u), 1 \leq q \leq M_R$.

Obviously, $\boldsymbol{s}_{ypc}(t_q, \eta_u)$ is thought of as the compressed signal vector $\boldsymbol{y}$ and $\boldsymbol{S}_{pc}(t_q, f_a)$ as the full signal vector $\boldsymbol{x}$. The small size azimuth inverse Fourier transform matrix $\boldsymbol{\Phi}_{y\text{AIFT}}$ is understood to be the sensing matrix $\boldsymbol{A}$, which can be calculated as

$$\boldsymbol{\Phi}_{y\text{AIFT}} = \boldsymbol{\Phi}_{\text{AIFT}}\boldsymbol{\Lambda}_m\widehat{\boldsymbol{I}}_y \tag{48}$$

where the azimuth inverse Fourier transform matrix $\boldsymbol{\Phi}_{\text{AIFT}}$ consists of a series of row vectors $\boldsymbol{\phi}_i$

$$\boldsymbol{\Phi}_{\text{AIFT}} = \left[\boldsymbol{\phi}_1, \ldots, \boldsymbol{\phi}_{m_a}, \ldots, \boldsymbol{\phi}_{M_A}\right]^T, \ m_a = 1, 2, \ldots, M_A. \tag{49}$$

Obviously, the sizes of $\boldsymbol{\Phi}_{\text{AIFT}}$ and $\boldsymbol{\Phi}_{y\text{AIFT}}$ equal $M_A \times M_A$ and $M_A \times M_{NZ}$, respectively.

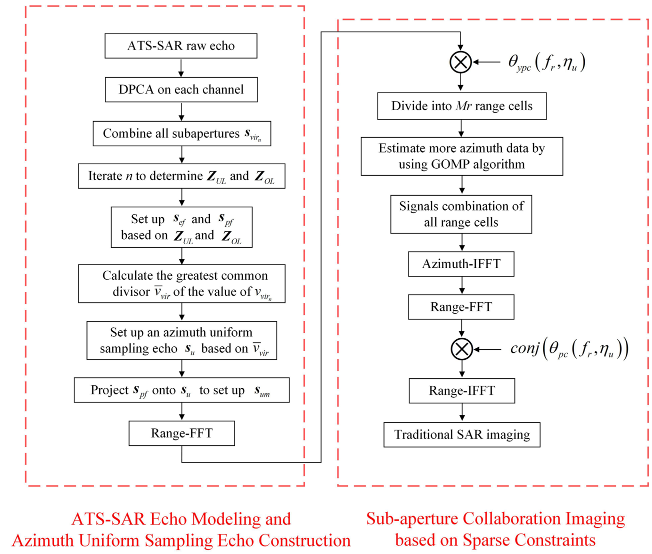

Fig. 7. Flowchart of the proposed SACIm-ATS algorithm.

Consequently, the entire signal recovery problem can be solved using the following formula:

$$\min_{\boldsymbol{S}_{pc}(t_q, f_a)} ||\boldsymbol{S}_{pc}(t_q, f_a)||_1$$
$$\text{s.t.} \quad ||\boldsymbol{S}_{pc}(t_q, f_a)\boldsymbol{\Phi}_{y\text{AIFT}} - \boldsymbol{s}_{ypc}(t_q, \eta_u)||_2 \leq \epsilon \tag{50}$$

where $||\cdot||_i$ and ϵ denote i-norm and the threshold parameter, respectively. Then, after the combination of all recovered 1-D signals, the estimated phase-compensated complete echo $\hat{\boldsymbol{S}}_{pc}(t, f_a)$ is obtained. To generate the estimation value of complete echo $\hat{\boldsymbol{s}}_u(t, \eta_u)$, the conjugation of aforementioned PCF should be compensated, and this step can be expressed as

$$\hat{\boldsymbol{S}}_u(f_r, \eta_u) = \hat{\boldsymbol{S}}_{pc}(f_r, \eta_u)\text{conj}\left(\boldsymbol{\theta}_{pc}\left(f_r, \eta_u\right)\right) \tag{51}$$

where conj$(\cdot)$ denotes the conjugate operation. Therefore, due to the accuracy estimation of full aperture data, the imaging performance of ATS-SAR can be significantly improved. In order to clearly demonstrate the ATS-SAR echo modeling step and the logic of the proposed SACIm-ATS algorithm, the algorithm flowchart is shown in Fig. 7.

Note that, if ATS-SAR contains a large number of aircrafts and their flight velocities are significantly different, the proposed algorithm may generate a large number of oversampling points, leading to an inaccurate estimated complete echo and incorrect imaging result. Hence, the proposed SACIm-ATS is more suitable for the small-scale ATS-SAR. Moreover, SACIm-ATS is literally a generalization of the SOA-AMDIA and embraces it as a special case when all platforms moving with the same velocities.

IV. Simulation Validation and Analysis

First, a one-input-five-output ATS-SAR is conducted to validate the effectiveness of the proposed SACIm-ATS. In this SIMO ATS-SAR, only platform 2 transmits the signal. Target 1 (−5, −5), Target 2 (5, −5), Target 3 (−5, 5), and Target 4 (5, 5) are

TABLE I
KEY PARAMETERS FOR SIMULATION

Parameters	Value
f_c: Central frequency	10 GHz
R_c: Shortest central slant range	50 km
B: Signal frequency bandwidth	150 MHz
f_s: Range sampling rate	180 MHz
F_a: Pulse repetition frequency	100 Hz
L_{fa}: Length of full aperture	1000 m
y_{vir_n}: Initial azimuth positions of virtual platforms	100/ 200/ 300/ 400/ 500 m

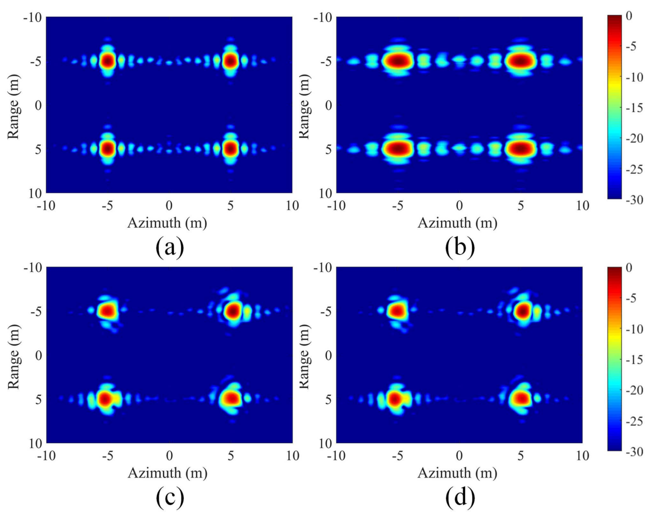

Fig. 8. When ideal formation case occurs, the imaging result obtained by (a) the BPA with the full echo, (b) the BPA with the ATS-SAR echo, (c) the SOA-AMDIA with the ATS-SAR echo, (d) the proposed SACIm-ATS with the ATS-SAR echo.

placed in the imaging scene. The related simulation parameters can be checked in Table I.

A. ATS-SAR Imaging in Ideal Formation Case

First, we assume that $v_{vir_1} = v_{vir_2} = v_{vir_3} = v_{vir_4} = v_{vir_5} = 100$ m/s to ensure the ATS-SAR is working in the ideal formation case. Fig. 8(a) shows imaging result obtained by the traditional Back-Projection Algorithm (BPA) with full aperture data, which is regarded as the ideal imaging result [31]. The rest of the subfigures of Fig. 8 demonstrate the imaging results obtained by BPA, SOA-AMDIA, and the proposed SACIm-ATS, with the ATS-SAR echo.

Due to the loss of azimuth data, Fig. 8(b) has a worse azimuth resolution than the ideal imaging result. In contrast, the SOA-AMDIA and the proposed SACIm-ATS can obtain better imaging results. Since the SOA-AMDIA is a particular case of the proposed SACIm-ATS in the ideal formation case, the imaging results of Fig. 8(c) and (d) are identical. Furthermore,

TABLE II
IMAGING PERFORMANCE PARAMETERS COMPARISON IN THE IDEAL FORMATION CASE

Imaging Algorithms	IRW (m)	PSLR (dB)	MVSL (dB)
BPA (Full Echo)	0.67	-11.51	-19.84
BPA (ATS-SAR Echo)	1.30	-12.98	-14.96
SOA-AMDIA	0.77	-12.40	-21.01
Proposed SACIm-ATS	0.77	-12.40	-21.01

since the SOA-AMDIA and the proposed SACIm-ATS algorithm aim at reconstructing the complete aperture data, there must be reconstruction errors between the real complete aperture data and the reconstructed one. The reconstruction error will result in slight phase error of the azimuth samples, affecting the final imaging result, such as the asymmetry.

The azimuth impulse response width (IRW) and the peak side-lobe ratio (PSLR) are measured for quantitative evaluation of imaging results. Since the high side-lobes generated by AMD-SAR might appear anywhere along the azimuth, the integrated side-lobe ratio (ISLR) may not accurately reflect the true image quality. Thus, a revised ISLR parameter named mean value of side-lobe (MVSL) is defined in this article, which can be expressed as

$$\mathrm{MVSL} = \mathrm{mean}\left(\sum_{q=1}^{Q} 10\lg\frac{|\mathrm{silo}(q)|}{|\max(\mathrm{silo})|}\right) \tag{52}$$

where $\mathrm{silo}(q)$ denotes the value of the qth side-lobe, Q represents the side-lobes number, and $\max(\mathrm{silo})$ is the value of the maximum side-lobe.

Then, the mean IRW, mean PSLR, and mean MVSL of four targets are demonstrated in Table II. The ideal values are marked in blue and the best values are marked in red. By observing Table II, SACIm-ATS dramatically improves the imaging performance of the ATS-SAR. The azimuth IRW can be advanced from 1.30 to 0.77 m, almost identical to the ideal imaging result. Additionally, the MVSL is greatly reduced, implying that the azimuth side lobes are generally significantly suppressed.

Next, to illustrate the superiority of the proposed algorithm for ATS-SAR, the imaging performance under various complex formation motion situations is investigated and analyzed.

B. ATS-SAR Imaging When Complex Formation Case 1 Exists

In this situation, let that $v_{vir_1} = 80$ m/s, $v_{vir_2} = 100$ m/s, $v_{vir_3} = 80$ m/s, $v_{vir_4} = 80$ m/s, $v_{vir_5} = 100$ m/s. Hence, the ATS-SAR echo s_{pf} is an azimuth nonuniform sampling signal. The imaging results obtained by different imaging algorithms are shown in Fig. 9.

Compared with the imaging result obtained by the traditional BPA with ATS-SAR echo, the SOA-AMDIA can still improve the imaging performance, as Fig. 9(b) and (c) shown, respectively. The side-lobes along the azimuth direction are decreased and the azimuth IRW is obviously improved. Moreover, the

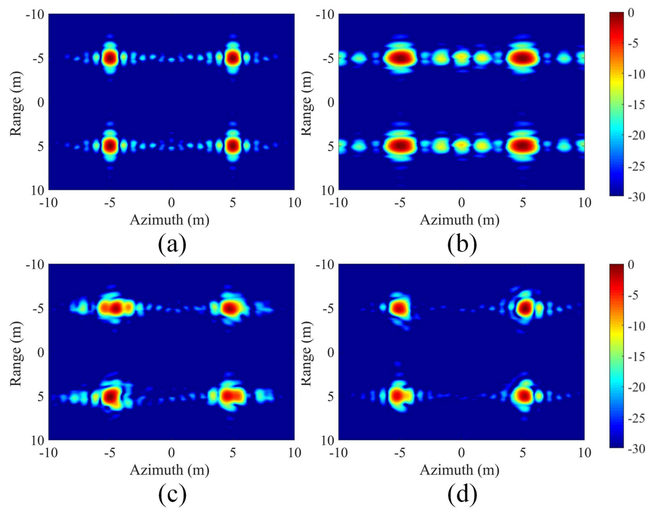

Fig. 9. When complex formation case 1 occurs, the imaging result obtained by (a) the BPA with the full echo, (b) the BPA with the ATS-SAR echo, (c) the SOA-AMDIA with the ATS-SAR echo, (d) the proposed SACIm-ATS with the ATS-SAR echo.

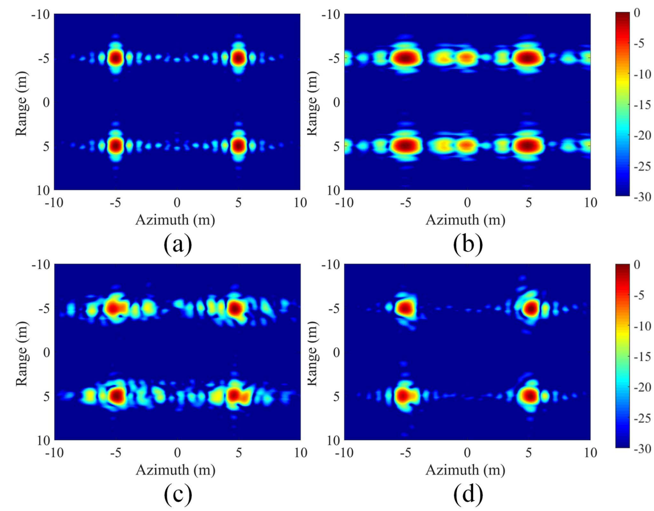

Fig. 10. When complex formation case 1 and 2 simultaneously exist, the imaging result obtained by (a) the BPA with the full echo, (b) the BPA with the ATS-SAR echo, (c) the SOA-AMDIA with the ATS-SAR echo, (d) the proposed SACIm-ATS with the ATS-SAR echo.

TABLE III
IMAGING PERFORMANCE PARAMETERS COMPARISON WHEN COMPLEX FORMATION CASE 1 EXISTS

Imaging Algorithms	IRW (m)	PSLR (dB)	MVSL (dB)
BPA (Full Echo)	0.67	-11.51	-19.84
BPA (ATS-SAR Echo)	1.31	-10.24	-15.92
SOA-AMDIA	0.91	-8.86	-17.62
Proposed SACIm-ATS	0.77	-11.90	-20.94

TABLE IV
IMAGING PERFORMANCE PARAMETERS COMPARISON WHEN COMPLEX FORMATION CASES 1 AND 2 SIMULTANEOUSLY EXIST

Imaging Algorithms	IRW (m)	PSLR (dB)	MVSL (dB)
BPA (Full Echo)	0.67	-11.51	-19.84
BPA (ATS-SAR Echo)	1.29	-9.61	-13.67
SOA-AMDIA	0.81	-8.44	-13.45
Proposed SACIm-ATS	0.77	-11.96	-20.75

proposed SACIm-ATS obtains the best imaging result under the condition of the nonuniform sampling ATS-SAR echo.

For a clearer illustration of the imaging performance differences among various imaging methods, Table III compares the relevant imaging performance characteristics. The ideal values are marked in blue and the best values are marked in red either. By observing Table III, the best azimuth IRW, PSLR, and MVSL are all obtained by the proposed SACIm-ATS. Compared with the SOA-AMDIA, the azimuth IRW can be increased 0.14 m using SACIm-ATS. The PSLR and MVSL are reduced 3.04 dB and 3.32 dB, respectively.

C. ATS-SAR Imaging When Complex Formation Case 1 and 2 Simultaneously Exist

Then, the echo configuration of ATS-SAR is further complicated. Assume that the complex formation case 1 and 2 simultaneously exist. In this case, let that $v_{vir_1} = 80$ m/s, $v_{vir_2} = 100$ m/s, $v_{vir_3} = 120$ m/s, $v_{vir_4} = 60$ m/s, $v_{vir_5} = 100$ m/s, which indicates that $L_{vir_1} = 80$ m, $L_{vir_2} = 100$ m, $L_{vir_3} = 120$ m, $L_{vir_4} = 60$ m, $L_{vir_5} = 100$ m. Clearly, $L_{vir_3} - L_{vir_4} < y_{vir_4} - y_{vir_3} < L_{vir_3}$ occurs between virtual subapertures 3 and 4, whereas other virtual subapertures are separated by gaps. The d_{vir_n} difference is more significant when complex formation cases 1 and 2 occur simultaneously. The imaging results are demonstrated in Fig. 10.

Comparing Fig. 10(c) with 9(c), the imaging results obtained by the SOA-AMDIA are deteriorating. Although the azimuth IRW obtained by the SOA-AMDIA is still superior to that obtained without any processing, it produces the worst sidelobes, resulting in the PSLR and MVSL being unacceptable. The proposed SACIm-ATS still focuses well, as shown in Fig. 10(d). It almost achieves an identical imaging performance to the BPA with full echo.

Table IV illustrates the comparison of the calculated azimuth IRW, PSLR, and MVSL. The azimuth IRW obtained by the SOA-AMDIA can still reach 0.81 m. However, its PSLR and MVSL are inadequate, only reaching -8.44 dB and -13.45 dB, indicating that the SOA imaging algorithm will no longer be excellent in this nonuniform sampling case. Conversely, the proposed SACIm-ATS can obtain an exceptional azimuth IRW along with the optimal PSLR and MVSL, which are 3.52 dB and 7.30 dB greater than the SOA-AMDIA, respectively. Thus, it is evident that the proposed SACIm-ATS algorithm is superior.

D. ATS-SAR Imaging When Complex Formation Case 1, 2, and 3 Simultaneously Exist

When complex formation case 1, 2, and 3 simultaneously exist, the echo configuration of ATS-SAR will be more complicated. In this case, assume that $v_{vir_1} = 80$ m/s, $v_{vir_2} =$

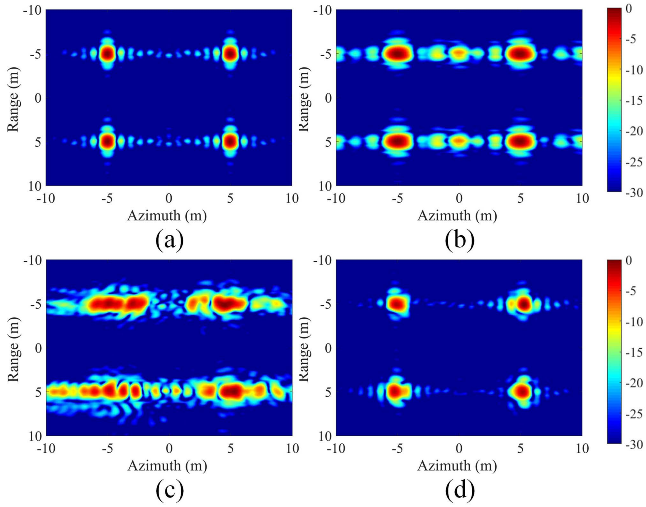

Fig. 11. When complex formation cases 1, 2, and 3 simultaneously exist, the imaging result obtained by (a) the BPA with the full echo, (b) the BPA with the ATS-SAR echo, (c) the SOA-AMDIA with the ATS-SAR echo, (d) the proposed SACIm-ATS with the ATS-SAR echo.

TABLE V
IMAGING PERFORMANCE PARAMETERS COMPARISON WHEN COMPLEX FORMATION CASES 1, 2, AND 3 SIMULTANEOUSLY EXIST

Imaging Algorithms	IRW (m)	PSLR (dB)	MVSL (dB)
BPA (Full Echo)	0.67	-11.51	-19.84
BPA (ATS-SAR Echo)	1.26	-8.04	-12.87
SOA-AMDIA	1.45	-2.62	-7.80
Proposed SACIm-ATS	0.77	-12.11	-20.24

100 m/s, $v_{vir_3} = 120$ m/s, $v_{vir_4} = 180$ m/s, $v_{vir_5} = 60$ m/s. Some azimuth data from virtual subapertures 3 and 4 overlap ($L_{vir_3} - L_{vir_4} < y_{vir_4} - y_{vir_3} < L_{vir_3}$), and virtual subaperture 5 is completely enclosed by virtual subaperture 4 ($0 < y_{vir_5} - y_{vir_4} \leq L_{vir_4} - L_{vir_5}$). The difference of d_{vir_n} becomes extremely worse. The imaging results obtained by four different imaging algorithms are illustrated in Fig. 11.

By observing Fig. 11(c), the SOA-AMDIA will no longer be able to obtain an accurate imaging result. There are multiple false targets in the final image. Moreover, a well-focused imaging result can still be obtained by the proposed SACIm-ATS algorithm, as shown in Fig. 11(d). Comparing with Figs. 8(d), 9(d), 10(d), and 11(d), the imaging performance of the proposed SACIm-ATS is not affected by the motion state of ATS-SAR. Thus, the effectiveness of the proposed SACIm-ATS has been fully verified. The SACIm-ATS can achieve an outstanding imaging performance for ATS-SAR, even in highly complex formation cases.

By observing Table V, the SOA-AMDIA is completely failed in the complex ATS-SAR echo situation. The azimuth IRW equals 1.45 m, even twice worse than that of the imaging result obtained by the BPA with full echo. On the contrary, compared with the imaging result obtained by the BPA with the ATS-SAR echo, the proposed SACIm-ATS algorithm can improve the azimuth IRW, PSLR, and MVSL by 39%, 51%, and 57%, respectively, reaching 0.77 m, -12.11 dB, and -20.24 dB, respectively. It implies that the proposed SACIm-ATS has a considerable advantage for the ATS-SAR imaging.

E. ATS-SAR Imaging Performance Effects of Different Echo SNRs

In order to further investigate the effectiveness of the proposed SACIm-ATS algorithm in the noisy environment, a series of simulations are designed in different echo SNR cases. The formation type of the ATS-SAR is identical to Section IV-D. The ATS-SAR imaging results obtained by the proposed SACIm-ATS algorithm in different echo SNR cases are demonstrated in Fig. 12. By observing Fig. 12(a), (b), and (c), the proposed SACIm-ATS algorithm obtains almost the same as that of the noise-free case shown in Fig. 11(d). When the echo SNR is equal to -5 and -10 dB, Target 2 $(5, -5)$'s azimuth IRW decreases and PSLR increases, as shown in Fig. 12(d) and (e). Meanwhile, by observing subfigures Fig. 12(f), (g), and (h), the worse echo SNR results in a rapid increase in the side lobes. Multiple false targets appear in the imaging scene, affecting the accuracy of the final images. Currently, the IRW and PSLR will not be enough to judge the quality of the imaging results. Therefore, two performance evaluation parameters, image entropy (IE) and image contrast (IC) are introduced. IE is expressed by

$$IE = -\sum_{l=1}^{L}\sum_{k=1}^{K} \frac{|\mathrm{Img}(l,k)|^2}{S} \ln \frac{|\mathrm{Img}(l,k)|^2}{S} \tag{53}$$

where

$$S = \sum_{l=1}^{L}\sum_{k=1}^{K} |\mathrm{Img}(l,k)|^2 \tag{54}$$

$\mathrm{Img}(l,k)$ denotes the value of image and the size of image is $L \times K$. IC can be expressed as

$$IC = \frac{\mathrm{std}\left(\mathrm{Img}(l,k)\right)}{\mathrm{mean}\left(\mathrm{Img}(l,k)\right)} \tag{55}$$

where $\mathrm{std}(\cdot)$ and $\mathrm{mean}(\cdot)$ represent the standard deviation and the mean value of the image. When IE is smaller or IC is larger, the quality of the image is superior.

The IC and IE results of ATS-SAR images obtained by the proposed SACIm-ATS algorithm in different SNR cases are shown in Fig. 13(a) and (b), respectively. All results are calculated by 100 times Monte-Carlo trails. Obviously, a better echo SNR environment ensures the imaging performance of the proposed SACIm-ATS algorithm. The median IC and median IE can reach 9.47×10^{-2} and 2.27, respectively, when echo SNR $= 5$ dB, which are very close to the ideal results. When the echo SNR ≤ 0 dB, both IE and IC results degrade remarkably. Moreover, although the maximum IE and IC are relatively close to the optimal results when echo SNR $\in (-20, -5)$ dB, their stability drops significantly. However, compared with the Fig. 11(c), even in a strong noisy environment, the proposed SACIm-ATS algorithm is able to provide superior imaging performance. When

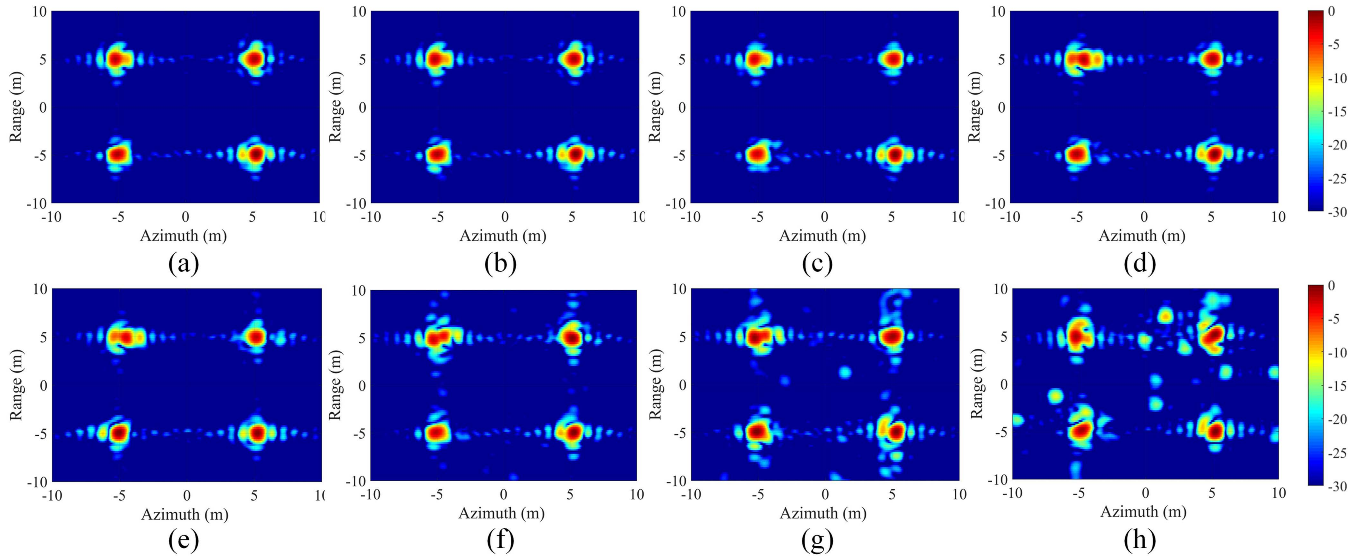

Fig. 12. ATS-SAR imaging results obtained by the proposed SACIm-ATS algorithm when echo (a) SNR = 10 dB; (b) SNR = 5 dB; (c) SNR = 0 dB; (d) SNR = −5 dB; (e) SNR = −10 dB; (f) SNR = −15 dB; (g) SNR = −20 dB; (h) SNR = −25 dB.

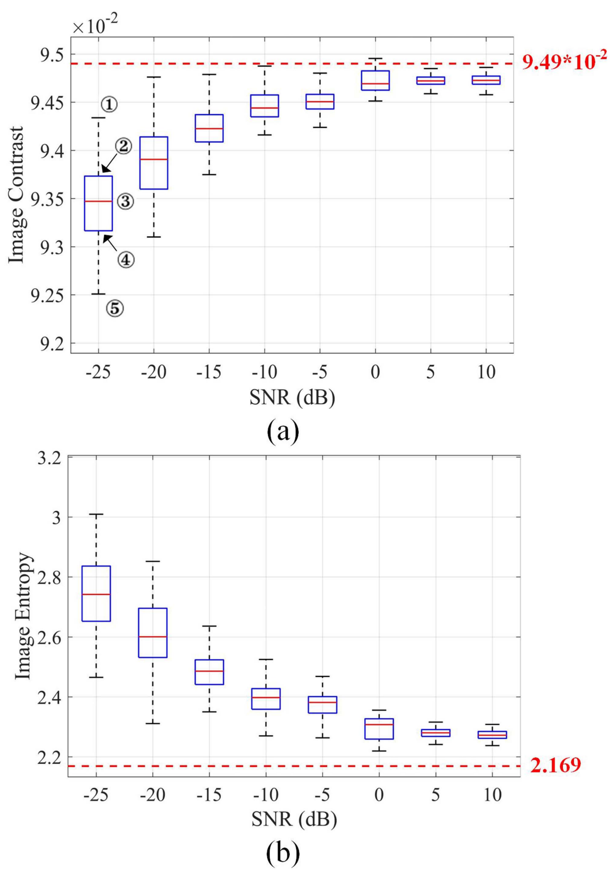

Fig. 13. (a) IC results of the ATS-SAR images obtained by the proposed SACIm-ATS algorithm in different SNR cases, where the red dotted line represents the IC result obtained by BPA with full echo without noise. Marker ① denotes the maximum value, ② denotes the 75% percentile value, ③ denotes the median value, ④ denotes the 25% percentile value, and ⑤ denotes the minimum value. (b) IE results of the ATS-SAR images obtained by the proposed SACIm-ATS algorithm in different SNR cases, where the red dotted line represents the IE result obtained by BPA with full echo without noise.

TABLE VI
KEY PARAMETERS FOR MMW-SAR EXPERIMENT

Parameters	**Value**
f_c: Central frequency	77 GHz
B: Signal frequency bandwidth	2.56 GHz
f_s: Range sampling rate	10 MHz
F_a: Pulse repetition frequency	100 Hz
M_R: Number of range samples	1024
M_A: Number of azimuth samples	1639
v_{mmw}: Velocity of MMW-radar	2.13 cm/s
d_{mmw}: Azimuth sampling interval	0.11 cm

the echo SNR drops to −25 dB, the best imaging result obtained by the proposed SACIm-ATS algorithm is still far inferior to the ideal result, indicating that the proposed algorithm is invalid.

V. ATS-SAR EXPERIMENT VALIDATION AND ANALYSIS

Obviously, no ATS-SAR measured data are currently available. To further verify the effectiveness of the proposed algorithm in the real scenarios, an artificial ATS-SAR data are generated from a real measured monostatic 77 GHz MilliMeter-Wave SAR (Mono-MMW-SAR) data [32]. The utilized MMW-radar and the imaging scenario are illustrated in Fig. 14(a) and (b), respectively. The related experimental parameters are demonstrated in Table VI.

In order to effectively simulate the ATS-SAR data from the Mono-MMW-SAR data, the azimuth data are resampled, which is shown in Fig. 15. Specifically, four equivalent subapertures are extracted from the original Mono-SAR data, and regarded

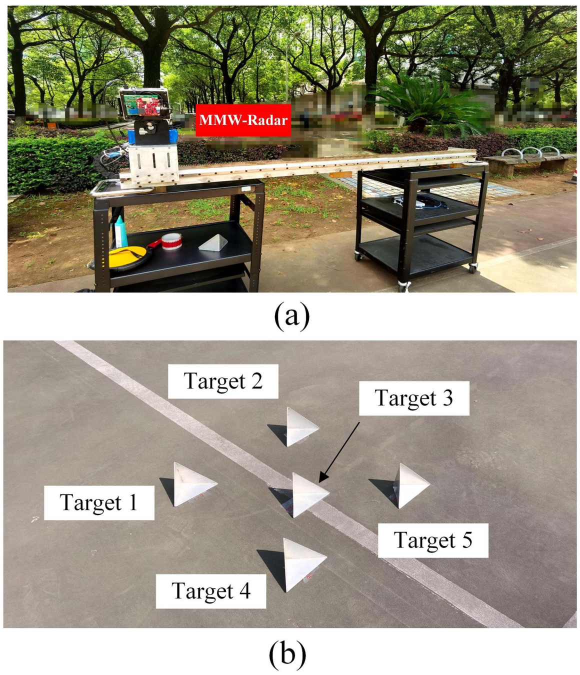

Fig. 14. (a) 77 GHz MMW-radar for the real measured Mono-SAR experiment. The length of electric track equals 1.57 m and the height of the MMW-radar equals 1.40 m. (b) Imaging scenario, which consists of five triangle reflectors. They are Target 1 (10.24, −0.18), Target 2 (10.24, 0.18), Target 3 (10, 0), Target 4 (9.83, −0.19), and Target 5 (9.85, 0.16).

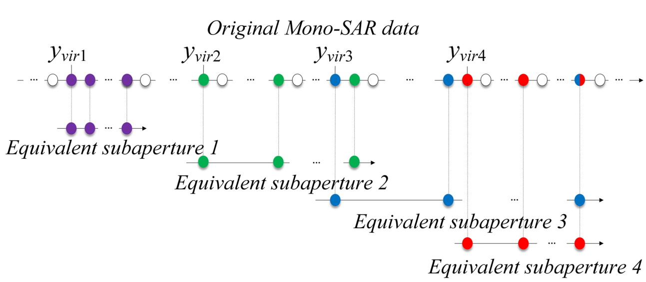

Fig. 15. Resampling the real measured Mono-SAR data to generate the ATS-SAR data. The generated ATS-SAR data consist of four equivalent subapertures, where $d_{vir1} = d_{mmw}$, $d_{vir2} = 5d_{mmw}$, $d_{vir3} = 10d_{mmw}$, and $d_{vir4} = 4d_{mmw}$.

as four received echoes of an ATS-SAR system. The speeds of the four equivalent SAR platforms are: $v_{vir1} = v_{mmw}$, $v_{vir2} = 5v_{mmw}$, $v_{vir3} = 10v_{mmw}$, and $v_{vir4} = 4v_{mmw}$. Hence, complex formation cases 1, 2, 3 simultaneously exist. The imaging results obtained by the aforementioned four different imaging algorithms, BPA with full echo, BPA with ATS-SAR echo, SOA-AMDIA with ATS-SAR echo, and the proposed SACIm-ATS algorithm, are demonstrated in Fig. 16(a)–(d), respectively.

First, five targets can be imaged using BPA with the full original Mono-MMW-SAR echo, as shown in Fig. 16(a). Targets 1 and 2 have lower energies since they are further away and somewhat obscured by the other targets in front of them. Then, by observing Fig. 16(b) and (c) can receive the same conclusion as Section IV. Due to the part of Doppler missing,

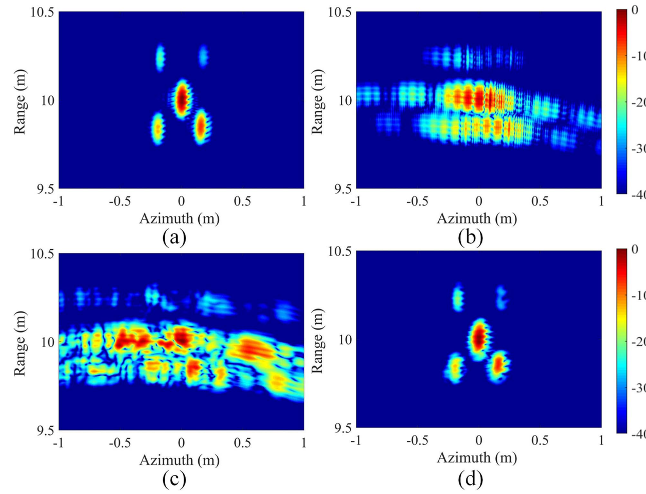

Fig. 16. Imaging result obtained by (a) the BPA with the full original Mono-MMW-SAR echo, (b) the BPA with the artificial ATS-SAR echo, (c) the SOA-AMDIA with the artificial ATS-SAR echo, (d) the proposed SACIm-ATS with the artificial ATS-SAR echo.

TABLE VII
IE AND IC RESULTS CORRESPONDING TO THE MEASURED DATA IMAGES

Imaging Algorithms	**IE**	**IC**
BPA (Full Echo)	1.729	0.095
BPA (ATS-SAR Echo)	3.352	0.090
SOA-AMDIA	3.910	0.086
Proposed SACIm-ATS	1.782	0.095

significant azimuth aliasing occurs if BPA is used directly with the ATS-SAR echo. Additionally, due to the nonuniform azimuth sampling intervals of the ATS-SAR echo, the SOA-AMDIA cannot reconstruct the ideal imaging result either. Compared with the BPA and the SOA-AMDIA, the proposed SACIm-ATS significantly enhances the imaging quality, obtaining five well-focused targets, as shown in Fig. 16(d). To effectively quantify and compare the imaging performance of the subfigures in Fig. 16, Table VII concludes the IE and IC results corresponding to the measured data images. We also mark the ideal values in blue and the best results in red.

Obviously, compared with the SOA-AMDIA, the proposed SACIm-ATS algorithm achieves the optimal imaging quality, whose IE and IC are equal to 1.782 and 0.095, respectively. They are very close to the ideal value, which are equal to 1.729 and 0.095. Therefore, the effectiveness of the proposed SACIm-ATS has also been verified in the real scenario. Its superiority is fully demonstrated.

VI. Conclusion

In this article, a new concept ATS-SAR was proposed and investigated. ATS-SAR aims to reduce data collection time while obtaining azimuth high resolution. First, considering the practical motion state difference of each individual platform, multiple

ATS-SAR echo models are established. Then, a corresponding ATS-SAR collaboration imaging algorithm, SACIm-ATS, was developed based on the sparse constraints. The proposed algorithm can accurately estimate the full Doppler bandwidth from the ATS-SAR echo. The simulations and an artificial real measured ATS-SAR experiment demonstrated that the imaging performance of the proposed algorithm is not affected by the platform's velocity difference of ATS-SAR. Compared to the SOA imaging method, the proposed SACIm-ATS yields nearly identical imaging results to those of perfect pictures.

Moreover, several directions may be further explored since ATS-SAR is a new concept. 1) Extend ATS-SAR to the form of arbitrary orbit formation. In the case of arbitrary trajectory formation, the arbitrary swarm SAR will have greater degrees of freedom, stronger flexibility and concealment. 2) Use ATS-SAR to image moving targets. ATS-SAR has outstanding advantages in imaging moving targets. First, due to its short data acquisition time, the motion changes of moving targets are small in a short time, and the motion of the moving targets is easier to model. At the same time, the ATS-SAR can increase the dimensions of observing moving targets. Thus, it can more accurately estimate the multidimensional motion speed of moving targets. 3) ATS-SAR can be further upgraded to MIMO mode, allowing different radar to emit different optimized waveforms [33], [34]. It can increase the observation dimensions by obtaining high resolution and combining the advantages of different waveforms to obtain more information in the imaging scene.

Appendix

In this appendix, the applicability of the Taylor approximation expansion is derived. First, γ is defined as

$$\gamma \triangleq (v_n - v_t)\,\eta + I_n \tag{56}$$

to facilitate the following derivation. Then, the slant range difference between the bistatic and monostatic SAR can be expressed as

$$\boldsymbol{R}_t + \boldsymbol{R}_{r_n} - 2\boldsymbol{R}_{vir_n} = \frac{\gamma^2}{4R_0} - \frac{\gamma^4}{64R_0^3} + \frac{\gamma^6}{512R_0^5} + o(\gamma). \tag{57}$$

Therefore, the phase error $\Delta\varphi$ is expressed as

$$\begin{aligned}\Delta\varphi &= \frac{2\pi}{\lambda}\left(\boldsymbol{R}_t + \boldsymbol{R}_{r_n} - 2\boldsymbol{R}_{vir_n}\right)\\ &\approx \frac{\pi\gamma^2}{2\lambda R_0} - \frac{\pi\gamma^4}{32\lambda R_0^3} + \frac{\pi\gamma^6}{256\lambda R_0^5} + \cdots.\end{aligned} \tag{58}$$

1) Far-field Standard: Obviously, if the second-order expansion satisfies $|\pi\gamma^2/2\lambda R_0| \le \pi/2$, the ATS-SAR can be seen as working in the far-field case. Thus, the far-field standard of γ can be obtained, that is, $\gamma \le \sqrt{\lambda R_0}$. In this case, the second-order expansion of $\Delta\varphi$ can be ignored. When the moving velocity of individual platform is not much different, the interval I_n can be regarded as $I_n \approx \gamma \le \sqrt{\lambda R_0}$.

2) Applicability of Expansion Item: The azimuth resolution ρ_a can be calculated by

$$\rho_a \approx 0.886 * \frac{\lambda R_0}{2L_{fa}}. \tag{59}$$

In the ATS-SAR, the complete synthetic aperture length L_{fa} is obvious larger than $\max I_n$. Therefore, (59) can be further expressed as

$$\rho_a \approx 0.886 * \frac{\lambda R_0}{2L_{fa}} > 0.886 * \frac{\lambda R_0}{2\max I_n}. \tag{60}$$

Next, the applicability of the expansion item can be derived based on (60).

Firstly, in the far-field case, the azimuth resolution requirements corresponding to the second-order expansion is that

$$\rho_a > 0.886 * \frac{\sqrt{\lambda R_0}}{2} \tag{61}$$

since $\max I_n = \sqrt{\lambda R_0}$.

Second, when the second-order expansion $\Delta\varphi$ does not meet the azimuth focus condition, it should be compensated. Then, the focus effect of $\Delta\varphi$'s third-order expansion should to be analyzed. The applicable scope of I_n can be obtained, that is

$$\left|\frac{\pi\gamma^4}{32\lambda R_0^3}\right| \le \frac{\pi}{2} \Longrightarrow I_n \approx \gamma \le 2R_0\sqrt[4]{\frac{\lambda}{R_0}}. \tag{62}$$

Therefore, the azimuth resolution requirements of the third-order expansion is that

$$\rho_a > 0.886 * \frac{\sqrt[4]{\lambda^3 R_0}}{4}. \tag{63}$$

It implies that when ρ_a satisfies (63), the third-order expansion can be ignored after the second-order phase compensation.

Third, if the second- and third order do not meet the azimuth focus condition, the analysis of $\Delta\varphi$ should be expanded to fourth order. The applicable scope of I_n is obtained by

$$\left|\frac{\pi\gamma^6}{256\lambda R_0^5}\right| \le \frac{\pi}{2} \Longrightarrow I_n \approx \gamma \le 2R_0\sqrt[6]{\frac{2\lambda}{R_0}}. \tag{64}$$

Next, the resolution limits of the fourth-order expansion can be expressed as

$$\rho_a > 0.886 * \frac{1}{4}\sqrt[6]{\frac{\lambda^5 R_0}{2}}. \tag{65}$$

When ρ_a satisfies (65), the fourth-order expansion can be ignored after the second- and third-order phase compensation. In fact, the second- or third-order expansion of $\Delta\varphi$ can already handle most ATS-SAR imaging requirements. Finally, for a higher resolution requirement, $\Delta\varphi$ should preserve higher order terms and be phase compensated.

References

[1] W. M. Brown, "Synthetic aperture radar," *IEEE Trans. Aerosp. Electron. Syst.*, no. 2, pp. 217–229, Mar. 1967.
[2] B. Zhang, W. Hong, and Y. Wu, "Sparse microwave imaging: Principles and applications," *Sci. China Inf. Sci.*, vol. 55, no. 8, pp. 1722–1754, 2012.
[3] K. Ouchi, "Recent trend and advance of synthetic aperture radar with selected topics," *Remote Sens.*, vol. 5, no. 2, pp. 716–807, 2013.

[4] D. L. Donoho, “Compressed sensing,” *IEEE Trans. Inf. Theory*, vol. 52, no. 4, pp. 1289–1306, Apr. 2006.
[5] E. J. Candès, J. Romberg, and T. Tao, “Robust uncertainty principles: Exact signal reconstruction from highly incomplete frequency information,” *IEEE Trans. Inf. theory*, vol. 52, no. 2, pp. 489–509, Feb. 2006.
[6] J. Yang, J. Thompson, X. Huang, T. Jin, and Z. Zhou, “Random-frequency SAR imaging based on compressed sensing,” *IEEE Trans. Geosci. Remote Sens.*, vol. 51, no. 2, pp. 983–994, Feb. 2013.
[7] H. Bi, G. Bi, B. Zhang, W. Hong, and Y. Wu, “From theory to application: Real-time sparse SAR imaging,” *IEEE Trans. Geosci. Remote Sens.*, vol. 58, no. 4, pp. 2928–2936, Apr. 2020.
[8] W. Pu, “Deep SAR imaging and motion compensation,” *IEEE Trans. Image Process.*, vol. 30, pp. 2232–2247, 2021.
[9] N. Gebert, “Multi-channel azimuth processing for high-resolution wide-swath SAR imaging,” 2009. [Online]. Available: https://elib.dlr.de/59686/
[10] B. Osmanoglu, F. Sunar, S. Wdowinski, and E. Cabral-Cano, “Time series analysis of InSAR data: Methods and trends,” *ISPRS J. Photogrammetry Remote Sens.*, vol. 115, pp. 90–102, 2016.
[11] A. Currie and M. A. Brown, “Wide-Swath SAR,” in *IEE Proc. F (Radar Signal Process.)*, vol. 139, pp. 122–135, 1992.
[12] G. Callaghan and I. Longstaff, “Wide-swath space-borne SAR using a quad-element array,” *IEE Proc.-Radar, Sonar Navigation*, vol. 146, no. 3, pp. 159–165, 1999.
[13] X. Zhang, H. Wu, H. Sun, and W. Ying, “Multireceiver SAS imagery based on monostatic conversion,” *IEEE J. Sel. Topics Appl. Earth Observ. Remote Sens.*, vol. 14, pp. 10835–10853, 2021.
[14] Y. Zou, Z. Zhou, X. Dong, and Z. Meng, “Distributed formation control for multiple verticaltakeoff and landing UAVs with switching topologies,” *IEEE/ASME Trans. Mechatron.*, vol. 23, no. 4, pp. 1750–1761, Aug. 2018.
[15] A. Puente-Castro, D. Rivero, A. Pazos, and E. Fernandez-Blanco, “A review of artificial intelligence applied to path planning in UAV swarms,” *Neural Comput. Appl.*, vol. 34, pp. 153–170, 2021.
[16] Z. Fang, Z. Li, X. Mao, Y. Yang, J. Wu, and J. Yang, “A time-domain image formation for high frame rate UAV swarm SAR,” in *Proc. IEEE Int. Geosci. Remote Sens. Symp.*, 2022, pp. 2506–2509.
[17] G. Krieger and A. Moreira, “Spaceborne bi-and multistatic SAR: Potential and challenges,” *IEE Proc.-Radar, Sonar Navigation*, vol. 153, no. 3, pp. 184–198, 2006.
[18] P. Guccione, A. Monti Guarnieri, F. Rocca, D. Giudici, and N. Gebert, “Along-track multistatic synthetic aperture radar formations of minisatellites,” *Remote Sens.*, vol. 12, no. 1, pp. 1–23, 2020.
[19] A. Renga, M. D. Graziano, and A. Moccia, “Formation flying SAR: Analysis of imaging performance by array theory,” *IEEE Trans. Aerosp. Electron. Syst.*, vol. 57, no. 3, pp. 1480–1497, Jun. 2021.
[20] N. Jiang, J. Wang, D. Feng, N. Kang, and X. Huang, “SAR imaging method for moving target with azimuth missing data,” *IEEE J. Sel. Topics Appl. Earth Observ. Remote Sens.*, vol. 15, pp. 7100–7113, 2022.
[21] Y. Qian and D. Zhu, “High-resolution SAR imaging from azimuth periodically gapped raw data via generalised orthogonal matching pursuit,” *Electron. Lett.*, vol. 54, no. 21, pp. 1235–1237, 2018.
[22] J. Wang, S. Kwon, and B. Shim, “Generalized orthogonal matching pursuit,” *IEEE Trans. Signal Process.*, vol. 60, no. 12, pp. 6202–6216, Dec. 2012.
[23] K. Liu, W. Yu, and J. Lv, “Azimuth interrupted FMCW SAR for high-resolution imaging,” *IEEE Geosci. Remote Sens. Lett.*, vol. 19, 2020, Art. no. 4001105.
[24] K. Liu, W. Yu, J. Lv, and Z. Tang, “Parameter design and imaging method of spaceborne azimuth interrupted FMCW SAR,” *IEEE Geosci. Remote Sens. Lett.*, vol. 19, 2022, Art. no. 4015505.
[25] J. Wu, D. Feng, J. Wang, and X. Huang, “SAR imaging from azimuth missing raw data via sparsity adaptive StOMP,” *IEEE Geosci. Remote Sens. Lett.*, vol. 19, 2022, Art. no. 4501605.
[26] N. Jiang, D. Feng, J. Wang, and X. Huang, “Missing data SAR imaging algorithm based on two dimensional frequency domain recovery,” in *Proc. IEEE Int. Geosci. Remote Sens. Symp.*, 2022, pp. 2490–2493.
[27] N. Jiang, Q. Xin, J. Zhu, D. Feng, J. Wang, and X. Huang, “Enhancement synthetic aperture imaging algorithm with azimuth missing data,” *Electron. Lett.*, vol. 59, no. 2, 2023, Art. no. e12729.
[28] N. Jiang, J. Zhu, D. Feng, Z. Xie, J. Wang, and X. Huang, “High-resolution SAR imaging with azimuth missing data based on sub-echo segmentation and reconstruction,” *Remote Sens.*, vol. 15, no. 9, 2023, Art. no. 2428.
[29] L. Zhou et al., “Unambiguous reconstruction for multichannel nonuniform sampling SAR signal based on image fusion,” *IEEE Access*, vol. 8, pp. 71558–71571, 2020.
[30] C. Hu, Z. Chen, X. Dong, and C. Cui, “Multistatic geosynchronous SAR resolution analysis and grating lobe suppression based on array spatial ambiguity function,” *IEEE Trans. Geosci. Remote Sens.*, vol. 58, no. 9, pp. 6020–6038, Sep. 2020.
[31] X. Zhang, P. Yang, C. Tan, and W. Ying, “BP algorithm for the multireceiver SAS,” *IET Radar, Sonar Navigation*, vol. 13, no. 5, pp. 830–838, 2019.
[32] N. Jiang, H. Du, J. Wang, and X. Huang, “Experimental validation of 77 Ghz millimeter-wave SAR imaging with long integration time,” in *Proc. 5th Int. Conf. Digit. Signal Process.*, 2021, pp. 116–120.
[33] Z. Xie, Z. Xu, S. Han, J. Zhu, and X. Huang, “Modulus constrained minimax radar code design against target interpulse fluctuation,” *IEEE Trans. Veh. Technol.*, early access, doi: 10.1109/TVT.2023.3273206.
[34] Z. Xie, Z. Xu, C. Fan, S. Han, and X. Huang, “Robust radar waveform optimization under target interpulse fluctuation and practical constraints via sequential lagrange dual approximation,” *IEEE Trans. Aerosp. Electron. Syst.*, early access, doi: 10.1109/TAES.2023.3260814.

Nan Jiang received the B.S. degree in electronic information engineering and the M.S. degree in information and communication engineering from University of Electronic Science and Technology of China, Chengdu, China, in 2016 and 2019, respectively. He is currently working toward the Ph.D. degree in information and communication engineering with the National University of Defense Technology, Changsha, China. From 2018 to 2019, he was a visiting M.S. student with the Department of Engineering, University of Leicester, U.K.

His research interests include radar signal processing and compressed sensing.

Dong Feng received the B.S. degree in information engineering, and the M.S. and Ph.D. degrees in information and communication engineering from the National University of Defense Technology, Changsha, China, in 2013, 2015, and 2020, respectively.

He is currently a Lecturer with the National University of Defense Technology. His research interests include bistatic SAR image formation and holographic SAR 3-D image formation.

Jian Wang received the B.S., M.S., and Ph.D. degrees in information and communications engineering from National University of Defense Technology, Changsha, China, in 2003, 2004, and 2009, respectively.

He is currently a Lecturer with National University of Defense Technology. His research interests include ground surveillance radar, target tracking, SAR image formation, and SAR interferometry.

Jiahua Zhu received the B.S. degree in electronic engineering and Ph.D. degree in information and communication engineering from the National University of Defense Technology, Changsha, China, in 2012 and 2018, respectively. From 2015 to 2017, he was a visiting Ph.D. student with the School of Engineering, RMIT University, and the Department of Electrical and Electronic Engineering, University of Melbourne, Australia.

He is currently an Associate Professor with the College of Meteorology and Oceanography, National University of Defense Technology. His current research interests include waveform design and target detection for radar and sonar.

Dr. Zhu received the Best Paper Award in The 9th Research Symposium for Chinese PhD Students and Scholars in Australia, 2016, the Excellent Paper Award in 2021 IEEE/OES China Ocean Acoustics Conference, and the outstanding Ph.D. degree thesis of the Chinese People's Liberation Army (PLA), 2020. He was a technical committee member and an invited speaker of IEEE International Conference on Signal and Image Processing (ICSIP 2020), ICSIP2021 (Session Chair), and ICSIP2022 (Regional Chair of Changsha, China).

Xiaotao Huang (Senior Member, IEEE) received the B.S. and Ph.D. degrees in information and communications engineering from National University of Defense Technology, Changsha, China, in 1990 and 1999, respectively.

He is currently a Professor with National University of Defense Technology. His fields of interest include radar theory, signal processing, and radio frequency signal suppression.